AFRL-PR-WP-TR-2002-2062

MICROELECTROMECHANICAL SYSTEMS (MEMS)-BASED MICROCAPILLARY PUMPED LOOP FOR CHIP-LEVEL TEMPERATURE CONTROL

Jeffrey A. Kirshberg

University of California, Berkeley
336 Sproul Hall
Berkeley, CA 94270-5940

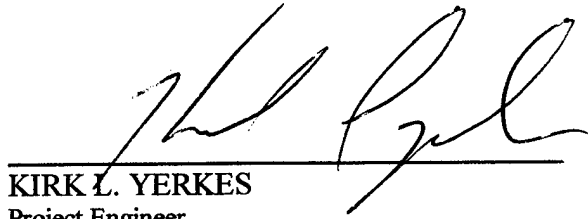**JANUARY 2002**

Final Report for 01 September 1997 – 01 January 2001

20020918 115

PROPULSION DIRECTORATE
AIR FORCE RESEARCH LABORATORY
AIR FORCE MATERIEL COMMAND
WRIGHT-PATTERSON AIR FORCE BASE, OH 45433-7251

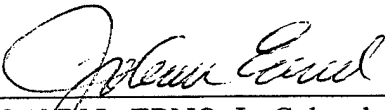This technical report has been reviewed and is approved for publication.

KIRK L. YERKES
Project Engineer
Power Division

BRIAN G. HAGER
Chief, Energy Storage & Thermal Sciences Branch
Power Division

JOANN L. ERNO, Lt Colonel, USAF
Deputy Chief
Power Division

REPORT DOCUMENTATION PAGE		Form Approved OMB No. 0704-0188

The public reporting burden for this collection of information is estimated to average 1 hour per response, including the time for reviewing instructions, searching existing data sources, searching existing data sources, gathering and maintaining the data needed, and completing and reviewing the collection of information. Send comments regarding this burden estimate or any other aspect of this collection of information, including suggestions for reducing this burden, to Department of Defense, Washington Headquarters Services, Directorate for Information Operations and Reports (0704-0188), 1215 Jefferson Davis Highway, Suite 1204, Arlington, VA 22202-4302. Respondents should be aware that notwithstanding any other provision of law, no person shall be subject to any penalty for failing to comply with a collection of information if it does not display a currently valid OMB control number. **PLEASE DO NOT RETURN YOUR FORM TO THE ABOVE ADDRESS.**

1. REPORT DATE *(DD-MM-YY)* January 2002	2. REPORT TYPE Final	3. DATES COVERED *(From - To)* 09/01/1997 – 01/01/2001

4. TITLE AND SUBTITLE MICROELECTROMECHANICAL SYSTEMS (MEMS)-BASED MICROCAPILLARY PUMPED LOOP FOR CHIP-LEVEL TEMPERATURE CONTROL	5a. CONTRACT NUMBER F33615-97-1-2788
	5b. GRANT NUMBER
	5c. PROGRAM ELEMENT NUMBER 62173C
6. AUTHOR(S) Jeffrey A. Kirshberg	5d. PROJECT NUMBER 1651
	5e. TASK NUMBER 01
	5f. WORK UNIT NUMBER 0G

7. PERFORMING ORGANIZATION NAME(S) AND ADDRESS(ES) University of California, Berkeley 336 Sproul Hall Berkeley, CA 94270-5940	8. PERFORMING ORGANIZATION REPORT NUMBER

9. SPONSORING/MONITORING AGENCY NAME(S) AND ADDRESS(ES) Propulsion Directorate Air Force Research Laboratory Air Force Materiel Command Wright-Patterson Air Force Base, OH 45433-7251	10. SPONSORING/MONITORING AGENCY ACRONYM(S) AFRL/PRPS
	11. SPONSORING/MONITORING AGENCY REPORT NUMBER(S) AFRL-PR-WP-TR-2002-2062

12. DISTRIBUTION/AVAILABILITY STATEMENT
Approved for public release; distribution is unlimited.

13. SUPPLEMENTARY NOTES
This report is a thesis.

14. ABSTRACT

Utilizing current microelectromechanical systems (MEMS) technologies, a three-port microcapillary pumped loop (micro-CPL) was designed, fabricated, and tested to provide integral cooling to electronics of MEMS-type devices. The two-wafer design consists of one silicon and one borofloat glass wafer. An analytical study, adopted from traditional CLP theory, was used in determining the geometry of the device, including the evaporator dimensions (1000 by 2000 μm) and the length of the liquid and vapor lines (35 mm). Using laser spot heating, the finished device was run near steady state. The micro-CPL resulted in a backside cooling effect of a least 7 K when a laser delivering 7.5 W (+/- 0.2 W) with a spot-size diameter of 1.0 mm was focused on the front side of the evaporator region.

15. SUBJECT TERMS
MEMS, capillary pumped loop, electronics cooling

16. SECURITY CLASSIFICATION OF:			17. LIMITATION OF ABSTRACT: SAR	18. NUMBER OF PAGES 112	19a. NAME OF RESPONSIBLE PERSON (Monitor) Kirk Yerkes
a. REPORT Unclassified	b. ABSTRACT Unclassified	c. THIS PAGE Unclassified			19b. TELEPHONE NUMBER *(Include Area Code)* (937) 255-5721

Standard Form 298 (Rev. 8-98)
Prescribed by ANSI Std. Z39-18

HES&S 31-15093-1

i

Table of Contents

List of Figures and Tables

Figure

Table

Acknowledgements

As I finish writing this thesis, I find myself reflecting over the past three and a half years. I cannot imagine what my graduate school experience would have been like without the guidance and support of my advisor, Professor Dorian Liepmann. It is with the highest honor that I call him my mentor.

This work could have never come to fruition had it not been for the vision and expertise of Dr. Kirk Yerkes. This research was driven by his insight, and it was my good fortune to learn from such a meticulous investigator.

This research was begun under a grant from the Scientific and Technology Research Program for BMDO, and is now supported by DARPA under its HERETIC program.

I was fortunate enough to interact with people who were constantly willing to share their expertise. With the aid of CFDRC, Dr. David Trebotich provided the numerical results in Chapter II. Professors Ralph Greif and Costas Grigoropoulos gave constant theoretical and experimental support. The fabrication was done at the Berkeley Sensor and Actuator Center, and would not have been possible except for the constant advice and support of its members, especially Jim Bustillo, John Evans, Uthara Srinivasan, Angad Singh and Alex Papavasiliou. The assistance and expertise of Don Reinmeuller in setting up the experiment at AFRL is thoroughly appreciated. The SEMs were captured by Ron Wilson, and all of my photolithographic masks were created by Marilyn Kushner. And for making the work seem like play, in addition to answering thousands of questions, I am extremely grateful for my lab-mates, Shilpa Shroff, Ajay

Deshmukh, Boris Stoeber, Jeff Zahn, Kenneth Pettigrew, Mike DeBar and Todd Weisgraber.

I also wish to thank a very special group of people who made my days in Berkeley so fulfilling. Dave Goldenberg, Jill Borut, Kelli Bundgard and Jen Scott always managed to keep me smiling, while showing me the idiocy of my ways. And since there are no words to thank a person for sharing their spirit, heart and dreams, I will honor Jeff Borut through my playing and searching . . . playing and searching.

Finally, I could never have earned my doctorate had it not been for the never-ending love and guidance of my family. Not only is their love unconditional, it is also inspirational. I pray that my every action reflects my parents' wisdom, my sister's dedication, and my brothers' acceptance. My education is as much a testament to their support, and the support of their parents, as it is to anything else.

Dedicated to Us.

"Ɛbe yɛ yie, Nyame beboa." – Ashanti saying

Chapter I. Introduction

I.1   Motivation

As the power supplied to electronic packages and Microelectromechanical Systems (MEMS) type devices increases, the question of thermal management becomes critical. The current mandate for power is reflected in everything from personal computer micro-processors to electronic packages required for unmanned aircraft. This, coupled with the demand for smaller systems, creates heat fluxes which become the most limiting factor in the production of micro-devices. Conventional methods of heat removal are simply not capable of dealing with the thermal gradients which lead to material failure. It therefore becomes necessary to look beyond traditional thermal management schemes, and develop techniques to deal with the cooling of micro-devices.

A micro-cooler based on MEMS technologies could be placed in direct contact with, or integrated directly into the micro-processor, sensor, or other electronic chip for which cooling is required and could maintain an optimal temperature. The advantages of this approach are three-fold. First, it allows for precise temperature control at the chip-level. Second, the overall cooling is more efficient because specific heat sources within the electronics package may be targeted. Third, the overall size of the electronic system can be kept small.

1

I.2   Background

The traditional heat pipe is one of the more efficient, traditional thermal

management systems in use today. As a closed system, it takes advantage of the

vaporization and condensation of its working fluid to transport heat from one end of the

pipe to the other. A heat pipe can be divided into three parts: an evaporator section, an

adiabatic section, and a condenser section, and is comprised of a sealed container, a wick

structure and a working fluid which is in equilibrium with its own vapor (Fahgri, 1995,

p.3). A schematic of a traditional heat pipe is shown in figure 1.1.
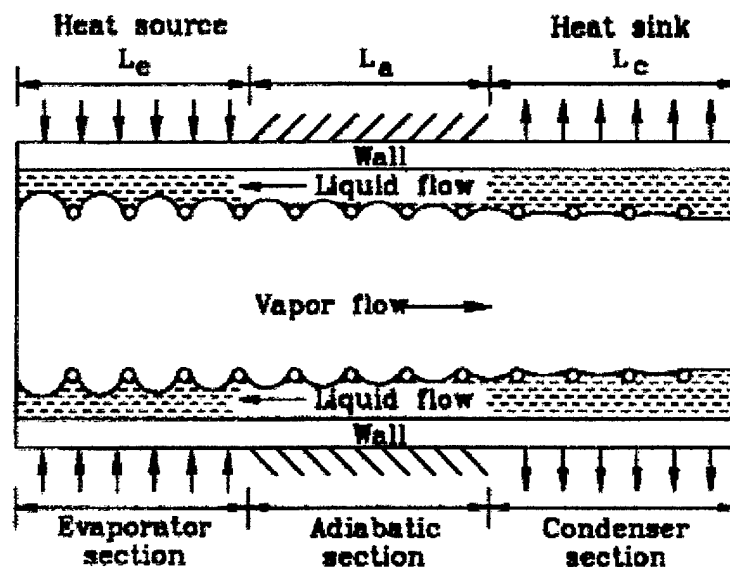
Figure 1.1 Schematic of a traditional heat pipe. (Fahgri, 1995, p.5)

Heat pipes are capable of passively transporting low heat fluxes as large amounts

of heat can be transported through small cross-sectional areas over large distances with

no additional power. "Heat, applied to the evaporator section by an external source is

2

conducted through the pipe wall and wick structure, where it vaporizes the working fluid. The resulting vapor pressure then drives the vapor through the adiabatic section to the condenser, where the vapor condenses, releasing the latent heat of vaporization to the provided heat sink. The capillary pressure created by the menisci in the wick pumps the condensed fluid back into the evaporator section. Therefore, the heat pipe can continuously transport the latent heat of vaporization from the evaporator to the condenser section." (Fahgri, 1995, p. 3)

The efficiency of a heat pipe can be understood by examining its effective thermal conductivity. "For example, a temperature difference of 900 C is needed to transfer 1 KW heat across a 30 mm diameter 1 m long copper rod. A heat pipe of the same size can transfer the same amount of heat with a temperature difference of less than 10 C. This indicates that the heat pipe can have a thermal conductivity 90 times higher than a copper bar of the same size." (Fahgri, 1995, p. 37-38) This small end to end temperature drop, coupled with the ability to control and transport large heat fluxes at different temperatures, makes the heat pipe a very effective form of thermal management.

Preparation of the device during start-up is essential for achieving efficient, steady state operation. The heat pipe is evacuated to remove the air within the system, and then filled with a pre-determined ratio of working fluid to working vapor, which exist in equilibrium within the heat pipe. The heat pipe is filled until the wick is saturated at the operating temperature of the pipe. Ideally, the entire temperature of the heat pipe should be increased (or decreased) from the ambient to the operating temperature before start-up, however this is seldom possible (Fahgri, 1995, p.35). Therefore, there usually exists a

ramp-up (or ramp-down) time when the heat pipe's temperature is shifting towards the saturation temperature of the working fluid. During this start-up, the heat entering the evaporator results in sensible heating (or cooling) of the working fluid prior to the onset of vaporization in the wicking structure. The length of time that the evaporator is operating in this sensible heating (or cooling) mode is dependent on the thermal mass of the heat pipe.

There are several, distinct operating limits which impact the rate of heat transport through a heat pipe. As Fahgri discusses in detail in his book Heat Pipe Science and Technology, there are eight limits to heat pipe operation, the lowest of which will determine the heat pipe's maximum transport potential. These limits are:

Capillary Pumping Limit – The ability of the capillary wicking structure to provide the pressure head necessary to power the closed loop cycle of the heat pipe. If the pressure losses due to friction in the heat pipe exceed the maximum capillary pressure that the wick can sustain, the wick will no longer be able to wet itself, resulting in wick dry-out. With only superheated vapor in the evaporator's wicking structure, temperatures in the evaporator will suddenly increase. This is the most common limit encountered in capillary driven heat pipes.

Sonic Limit – If the vapor speeds in the heat pipe approach the speed of sound, a choked flow condition can exist within the system limiting the overall mass flow rate and performance of the device.

Boiling Limit – If too much heat is supplied to the evaporator region, nucleate boiling will begin in the evaporator's wick structure. If low intensity boiling is exceeded, vapor bubbles can prevent liquid from wetting the pipe wall, resulting in wick dry-out.

Entrainment Limit – A shear force exists at the liquid/vapor interface along the wicking structure due to the counter-current flow within the heat pipe. At high enough velocities, governed by the Weber number, liquid droplets can be "torn" into the vapor space resulting in wick dry-out.

Vapor Pressure Limit – Viscous forces can become dominant at low operating temperatures, resulting in the vapor pressure at the condenser end approaching zero. This can limit the heat transport of the heat pipe.

Frozen Startup Limit – If the working fluid is initially frozen due to low ambient temperatures, the active length of the heat pipe at start-up will be less than the total length during steady-state operation, therefore not allowing operating at the capillary limit.

Condenser Heat Transfer Limit – If the heat fluxes deposited at the condenser end of the heat pipe are too high for the heat sink to remove, the heat pipe will be unable to perform at its maximum capacity.

Vapor Continuum Limit – If the length scales in the heat pipe are smaller than the mean free path of vapor at the operating temperature of the device, the heat pipe will be operating under a free molecular or rarified condition, which will impact the overall

performance of the heat pipe. This is most often encountered during frozen start-up, and is governed by the Knudsen number.

In 1961, Laub and McGinness began investigation into a slightly different type of two-phase thermal control system called a Capillary Pumped Loop (CPL). While they only examined a capillary pumped vapor generator, their work was later expanded on by Stenger in 1966, who reported on two CPLs capable of transporting more than 800 W over 50 ft. Since then, the CPL has been rigorously examined, and observed to be governed by the same limits as heat pipes. One–dimensional paradigms to design and predict their performance have been established (Dickey and Peterson, 1994). A schematic of a typical CPL is shown in figure 1.2.
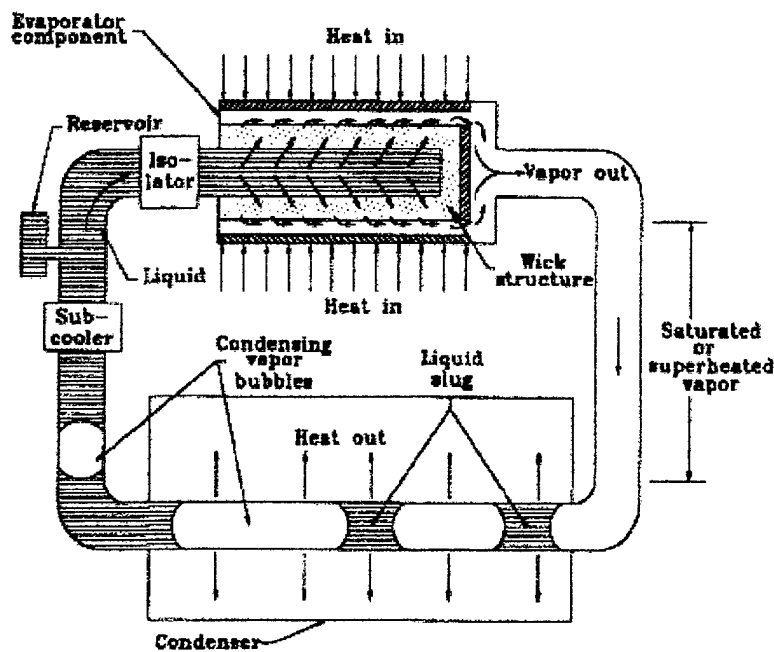
Figure 1.2 Schematic of a capillary pumped loop (CPL) (Fahgri, 1995, p.18)

Similar to heat pipes, the large effective thermal conductivity of a CPL is derived from the vaporization and condensation of its working fluid. "A major difference [between heat pipes and CPLs is that] the liquid and vapor flows are separated, thereby allowing for the vapor to be slightly superheated and the liquid to be slightly subcooled." (Dickey and Peterson, 1994). This allows the CPL to support larger temperature drops than a heat pipe, resulting in an overall lower effective thermal conductivity. However, because the vapor and liquid flows are now separated, and the wicking structure removed from a majority of the device, the pressure drops are reduced along the vapor and liquid lines, allowing for larger mass flow rates under the capillary pumping limit.

Control over the CPL operation is done through the working fluid reservoir. By pressurizing and heating (or cooling) the reservoir, the working pressure within the CPL can be altered. This has the effect of changing the saturation temperature of the working fluid, and therefore gives control over the operating temperature of the evaporator. This reservoir can be placed "far away" from the evaporator region, which allows for thermal isolation of the reservoir from the heat source driving the CPL.

Startup of a CPL differs from that of a traditional heat pipe. While they both need to be evacuated prior to filling in order to remove all non-condensable gases, the CPL is then completely flooded with the working fluid. Typically, heat is then applied to the liquid in the vapor line to begin evaporation, prior to heating the evaporator. If this is not done, the temperature in the evaporator region will spike up during start-up, as enough super heated vapor forms to push the liquid from the vapor line. This start-up temperature spike is avoided by "clearing" the vapor line prior to operation.

In the early 1980's another two-phase heat transfer device called the loop heat pipe was invented in Russia. Similar to the CPL, the vapor and liquid lines have been separated, allowing for co-current flow. "The LHP is known for its high pumping capability and robust operation because it uses fine-pored metal wicks and the integral evaporator/hydro-accumulator desing." (Ku, 1999, p.1) Since the reservoir, or hydro-accumulator, is imbedded into the evaporator, the loop heat pipe is much more robust during start-up. However, it is the location of the reservoir which also allows for less device control, compared to a CPL. Recall, that heating and pressurizing the reservoir allows for control over the saturation temperature within these devices. Embedding the reservoir in the evaporator region, as is done with the loop heat pipe, allows for less thermal isolation of the reservoir, and therefore less control over the operational temperature within the device. The CPL's thermal isolation of the reservoir makes it a more attractive choice for cooling electronic packages. A schematic of a loop heat pipe is shown in figure 1.3.
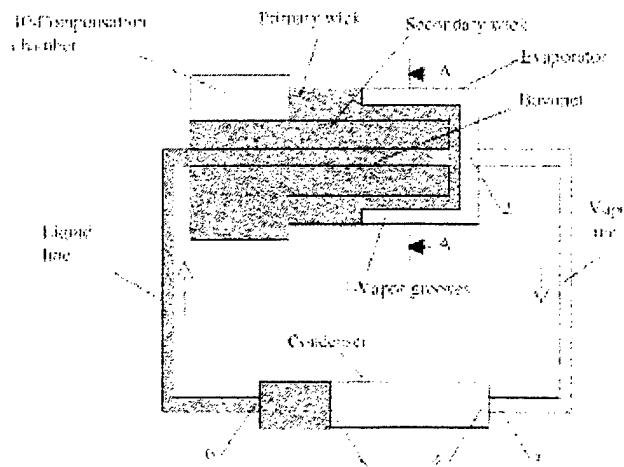
Figure 1.3 Schematic of a loop heat pipe. (Ku, 1995, p.2)

Having selected the CPL as the micro-cooler design, there are many challenges in transitioning MEMS technologies to this specific application. Specific technical challenges to the development of a micro-cooler include; (a) identification of potential micro-cooler thermodynamic processes, components, and geometries, (b) addressing the physics of micro scale heat transfer in solids, vapor, and liquids specific to the micro-cooler geometries, (c) addressing the physics of phase change phenomena in the micro scale regime, (d) the development of macro scale to micro scale scaling laws specific to the micro-cooler fluidic systems, (e) addressing system level benefits as well as interfacing between the micro- and macro-world, (f) modification of current or the development of new fabrication processes to allow the micro-cooler to be charged with the appropriate working fluid during fabrication, and (g) the development of appropriate calibration and testing diagnostics to verify the micro-cooler's performance.

CPLs possess several essential features which might make them more efficient micro-coolers than micro-capillary driven heat pipes. The co-current nature of their flow will allow for higher thermal loads, while their geometric flexibility will actually allow for heat to be transported from one region to another. In addition, CPLs are started by flooding the entire device, while heat pipes must be filled with a previously determined ratio of working fluid to working vapor. While this is feasible in macro-scale heat pipes, it becomes almost impossible to accomplish with the small volumes (on the order of 10^{-9} m^3) associated with micro-scale devices. Another distinct advantage of the CPL is the potential to further enhance the device's performance in conjunction with other major components. A thermal management system could consist of a new family of pumps and

valves to control liquid or vapor transport within the micro-CPL as well as innovative micro scale heat acquisition and heat rejection regions.

Micro-heat pipes have been analyzed rather extensively as potential micro-cooler configurations. Although the planar nature of micro-fabrication drastically alters the geometry and characteristics of any looped heat pipe, macro-scale heat pipe analysis has been successfully used in the development of its miniature and micro counterparts (Cao et. al., 1993). By spreading the heat, micro-heat pipes essentially have the effect of increasing the thermal conductivity of the targeted electronic package.

While attempts have been made to study potential wicking structures for a micro-CPL, no one had previously fabricated an entire device (Harms et al., 1999) (Holke et al., 1998). This thesis encompasses the initial design of a passive three-port micro-CPL, fabricated utilizing MEMS technologies. Following the paradigm driving micro heat pipe design, a one-dimensional analysis used previously on macro-scale CPLs was adopted for the micro-CPL's design. The validity of the design was confirmed by testing several designs, with different working fluids and heat sources. Table 1.1 shows a list of the experiments conducted.

Micro-CPL Design	Heat Source	Spot Size Diameter	Power Output	Orientation	Working Fluid	Hydrophobic Coating	Res. Pressure
First Generation	Micro-torch	Unknown	Unknown	Horizontal	Ethanol	No	15 psi
First Generation	Micro-torch	Unknown	Unknown	Horizontal	Water	No	15 psi
Second Generation	CO_2 Laser	3.5 mm	8.5 W (+/- 0.2 W)	Horizontal	Water	No	15 psi
Second Generation	CO_2 Laser	3.5 mm	8.5 W (+/- 0.2 W)	Vertical	Water	No	15 psi
None – Blank Wafers	CO_2 Laser	1.0 mm	7.5 W (+/- 0.2 W)	N/A	N/A	N/A	N/A
Second Generation	CO_2 Laser	1.0 mm	7.5 W (+/- 0.2 W)	Horizontal	Air	No	Amb
Second Generation	CO_2 Laser	1.0 mm	7.5 W (+/- 0.2 W)	Horizontal	Water	No	15 psi
Second Generation	CO_2 Laser	1.0 mm	7.5 W (+/- 0.2 W)	Horizontal	Water	Yes	15 psi

Table 1.1 Experiments performed on the micro-CPL

From the data obtained, the cooling performance of the micro-CPL was examined. Modes of operation within the evaporator were identified, and the impact of the small length scales present were observed. Finally, recommendations are made for future experiments to better quantify the micro-CPL's heat transfer characteristics.

Chapter II. Design

II.1   One Dimensional Capillary Pressure Limit

Adopting traditional CPL theory, the micro-CPL was designed to operate within distinct transport limits, in order to avoid device failure. Each of the eight limits listed in Chapter I was examined in order to determine the most dominate one. The limits of interest are determined by the operational temperature range of the device. The micro-CPL studied uses water as its working fluid with an assumed working temperature range between 333 K (60 C) and 413 K (140 C). In this range the capillary pumping limit will be the controlling limit of operation, with the boiling and condenser limits also influencing operation (Faghri, 1995, p.223). Full multi-dimensional solutions to these limits are extremely complex, so one-dimensional approximations are employed. Accordingly, the design of the first operational MEMS based micro-CPL is primarily based upon the capillary pumping limit.

Once the evaporator and condenser sizes of the micro-CPL are selected, most other geometric parameters become relatively fixed due to fabrication limitations. For example, the axial grooved wick structure is created by an isotropic wet etch utilizing polysilicon as the masking layer. As shown in figure 2.1, this results in a maximum groove width approximately twice the size of the groove depth. Therefore, an evaporative width of 500 μm can support four side by side 55 μm deep grooves, while maintaining flat borofloat glass between the grooves, a necessity for the final anodic bond. In

addition, the flat sidewalls needed for laminar flow in the liquid/vapor lines set their maximum depth to 150 μm, due to "undercutting" concerns during plasma etching. These issues are discussed in greater detail in Chapter III. Table 2.1 provides specifications for a micro-CPL with rectangular liquid/vapor line cross-sectional geometries, in addition to a planar evaporator and condenser with a grooved capillary wicking structure.
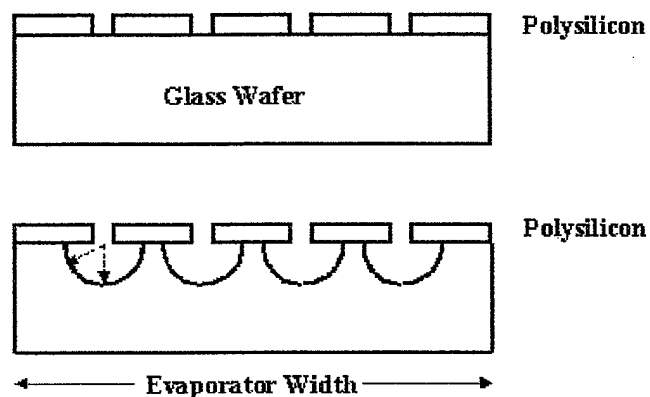
Figure 2.1 Wet etch of glass to form the axial grooved wicking structure sets certain geometric parameters

Evaporator Length	1000 μm
Evaporator Width	500 μm
Condenser Area	5.0e+05 sq. μm
Groove Height	55 μm
Groove Width	90 μm
Average Groove Radius	50 μm
Number of Grooves	4
Vapor Line Dimensions	150 x 450 μm
Liquid Line Dimensions	150 x 150 μm

Table 2.1 Micro-CPL Specifications

A parametric analysis of the micro-CPL Capillary Pumping Limit was conducted following the rationale of Dickey and Peterson (1994) while including the pressure drop of the vapor line. An energy balance of the evaporator region may be expressed as

$$Q_T = Q_{h_{fg}} + Q_{c_p \Delta T_{liq}} + Q_{c_p \Delta T_{vap}} \tag{2.1}$$

where Q_T is the total energy entering the evaporator region, $Q_{h_{fg}}$ is the phase change energy, and $Q_{c_p \Delta T}$ is the heating energy of the liquid or vapor. The energy required for the temperature change in the vapor is assumed small compared to the other terms. The liquid temperature change can be expressed as

$$Q_{c_p \Delta T} = \dot{m} c_p \left(T_s - T_l \right) \tag{2.2}$$

where T_l is the temperature of the liquid returning to the evaporator, and T_s is the saturation temperature of the working fluid. Since the liquid cooling occurs in the

14

condenser region, assuming adiabatic liquid and vapor lines, this temperature change can also be expressed as

$$Q_{c_p\Delta T} = A_c h_c \left(T_{w,c} - \left[\frac{(T_s + T_l)}{2} \right] \right)$$ (2.3)

where A_c is the surface area of the condenser, h_c is the convection coefficient of the working fluid, and $T_{w,c}$ is the condenser wall temperature. Setting (2.2) and (2.3) equal to each other, and solving for T_l yields

$$T_l = \frac{A_c h_c T_{w,c} - T_s \left[(A_c h_c / 2) + \dot{m} c_p \right]}{(A_c h_c / 2) - \dot{m} c_p}$$ (2.4)

Re-expressing the total energy entering the evaporator, (2.1), as

$$Q_T = \dot{m} h_{fg} + \dot{m} c_p (T_s - T_l)$$ (2.5)

and substituting in T_l, a quadratic expression for the mass flow rate can be expressed as

$$\dot{m}^2 \left(\frac{c_p h_{fg}}{A_c h_c} \right) + \dot{m} \left[h_{fg} + c_p T_s - \left(\frac{c_p Q_T}{A_c h_c} \right) - c_p T_{w,c} \right] - Q_T = 0$$ (2.6)

$$\bar{v} = \frac{\dot{m}}{\rho A}$$ (2.7)

Equation (2.6) must be satisfied while iteratively solving for the maximum mass flow rate which still satisfies the pressure relationship

$$\Delta P_c + \Delta P_l \geq \Delta P_w + \Delta P_l + \Delta P_v \qquad (2.8)$$

If the pressure losses exceed the pressure heads, the loop will stop operating, as the wick structure will no longer be able to wet itself. Each of the terms in equation (2.8) represent a particular geometric portion of the micro-CPL for which the pressure balance must be maintained for proper operation, and are assumed to have the following macro-scale relationships:

The capillary pressure drop across the liquid/vapor evaporation interface along the axial grooves is

$$\Delta P_c = \left(\frac{\sigma}{r_x} + \frac{\sigma}{r_y} \right) = \frac{\sigma}{r_g} \qquad (2.9)$$

where r_x equals r_g, the average radius of the grooves, and r_y approaches infinity. Equation (2.9) assumes the vapor/liquid interface shape illustrated in figure 2.2, which results from an evaporative cooling mode of operating within the evaporator (no bubbles present).
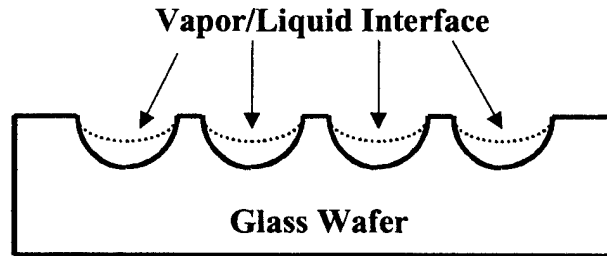
Figure 2.2 Shape of the liquid/vapor evaporation interface assumed to exist.

According to the Clausius-Clapeyron equation, the pressure drop due to the temperature gradient across this liquid/vapor interface is

$$\Delta P_I = \frac{h_{fg} P_v \Delta T}{R T_v^2} \qquad (2.10)$$

This expresses the pressure differential that exists between a subcooled liquid and its superheated vapor.

Assuming laminar flow, the pressure drop along the rectangular liquid line is

$$\Delta P_I = \rho \left(\frac{64}{\mathrm{Re}_I \left(\frac{2}{3} + \frac{11}{24} \left(\frac{h_I}{w_I} \right) \left(2 - \frac{h_I}{w_I} \right) \right)} \right) \left(\frac{L_I}{D_I} \right) \left(\frac{\bar{v}_I^2}{2} \right) \qquad (2.11)$$

where h_I, w_I, L_I, and D_I are the depth, width, length and hydraulic diameter of the liquid line respectively (Blevins, 1984).

Similarly, the pressure drop along the vapor line is

$$\Delta P_v = \rho \left(\frac{64}{\mathrm{Re}_v \left(\frac{2}{3} + \frac{11}{24} \left(\frac{h_v}{w_v} \right) \left(2 - \frac{h_v}{w_v} \right) \right)} \right) \left(\frac{L_v}{D_v} \right) \left(\frac{\bar{v}_v^2}{2} \right) \qquad (2.12)$$

The pressure drop experienced by the liquid filling the axial grooves in the evaporator region is found by integrating the momentum equation along the length of the grooves (Fahgri, 1995, pp. 124-127).

$$\Delta P_w = \int_0^{L_g} \frac{\mu_l \dot{m}_l}{\rho_l A_w K} \, dx = \int_0^{L_g} \frac{\mu_l Q_T}{\rho_l A_w K h_{fg}} \, dx$$

$$= \frac{\mu_l Q_T L_g}{\rho_l A_w K h_{fg}} \tag{2.13}$$

Again, this assumes an evaporative cooling mode of operation (no bubbles present) with liquid filling the bottom of the axial grooves, and a vapor interface all along the top of the liquid. In equation (2.13) the traditional macro-scale definition of wick permeability

$$K = \frac{2 \varepsilon r_{h,l}^2}{f_l \, \mathrm{Re}_l} = \frac{8 w (hw)^2 N_g}{f_l \, \mathrm{Re}_l \, w_l (2h+w)^2} \tag{2.14}$$

is used, where h, w, N_g and f_l are the groove height, groove width, number of grooves and friction factor respectively. Other traditional definitions like hydraulic radius,

$$r_{h,l} = \frac{2hw}{2h+w} \tag{2.15}$$

wick porosity for a non-circular axial groove,

$$\varepsilon = \frac{hwN_g}{hw_{evaporator}} = \frac{wN_g}{w_{evaporator}} \tag{2.16}$$

and the friction relationship (Shah and Bhatti, 1987),

$$f_l \, \mathrm{Re}_l = 24 \left(1 - 1.3553\alpha + 1.9467\alpha^2 - 1.7012\alpha^3 + 0.9564\alpha^4 - 0.2537\alpha^5 \right) \tag{2.17}$$

$$\alpha = \frac{w}{h} \tag{2.18}$$

18

were also used in this analytical approach.

II.2 First Generation Sensitivity Analysis

A Java program was created to balance the pressure relationship (2.8) for different vapor/liquid line lengths while solving equation (2.6) for the mass flow rate. With the evaporator and condenser sizes selected prior to the analysis, all other geometric parameters, excluding liquid/vapor line lengths, were fixed due to fabrication limitations. A sensitivity analysis of maximum total heat transport to liquid/vapor line length of the micro-CPL was performed. The program (Appendix A) iteratively solves equation (2.8) for different line lengths, therefore determining the maximum mass flow rate which the micro-CPL can support before reaching the capillary limit. The program then solves equation (2.6) for the rate allowed from heat transfer considerations, and checks that it is greater than the maximum flow rate allowed by the capillary pumping limit. Finally, the program examines the Reynolds number in both the liquid and vapor lines, guaranteeing that the channel flow remains laminar.

Several assumptions were made during this sensitivity analysis. While the axial grooves are parabolic, with a radius varying from 45 μm to 55 μm, they were assumed to be hemispherical with an average radius of 50 μm. The liquid/vapor lines were assumed to have flat sidewalls and bottoms, allowing for a laminar duct flow analysis. These lines were also assumed to be adiabatic, with heat transfer only occurring in the evaporator and condenser regions. Finally, a $3°$ sub-cooling was assumed in this analysis.

19

VARIABLE	DEFINITION	VALUE
C_p	Specific Heat of Water at T_s	4217 J/Kg-K
h_c	Coefficient of Natural Convection for Air	10 W/m^2-K
h_{fg}	Enthalpy of Evaporation for Water	2,257,000 J/Kg
μ_l	Viscosity of Liquid Water	0.000279 N-s/m^2
μ_v	Viscosity of Water Vapor	0.00001202 N-s/m^2
ρ_l	Density of Liquid Water	957.9 Kg/m^3
ρ_v	Density of Water Vapor	0.5956 Kg/m^3
P_v	Saturation Pressure at T_s	101330 Pa
R	Gas Constant for Water Vapor	461.3929 J/Kg-K
τ	Surface Tension of Water at T_s	0.0589 N/m
T_l	Liquid Water Temperature	370 K
T_s	Saturation Temperature of Water	373 K
$T_{w,c}$	Temperature of Condenser Wall	370 K

Table 2.2 Physical constants used in determining the micro-CPL geometry

Using the property values in table 2.2, and the fixed geometric parameters listed in table 2.1, estimates for the total heat transfer capability of the micro-CPL were calculated for different vapor/liquid line lengths. The computer output file can also be found in Appendix A. Figure 2.3 shows the results of the sensitivity analysis in a graph of liquid/vapor line length vs. total heat transfer for the micro-CPL. A liquid/vapor line length of 35 mm corresponds to a maximum heat transfer rate of 4 W, and was selected as the vapor/liquid line length. Table 2.3 summarizes the final geometric parameters of the first generation micro-CPL, including Reynolds numbers and maximum predicted heat transport.

Figure 2.3 Maximum transport distance based on the capillary pumping limit for the first generation micro-CPL

Evaporator Length	1000 μm
Evaporator Width	500 μm
Condenser Area	5.0e+05 sq. μm
Groove Height	55 μm
Groove Width	90 μm
Average Groove Radius	50 μm
Number of Grooves	4
Vapor Line Dimensions	150 x 450 μm
Liquid Line Dimensions	150 x 150 μm
Vapor/Liquid Line Length	35 mm
Liquid Line Re Number	26
Vapor Line Re Number	430
Projected Heat Removal	4 Watts

Table 2.3 Parameters of the first generation micro-CPL

Figure 2.4. A sketch of the micro-CPL. The fluidic channels (gray) are fabricated from silicon, while the wicking structure (white) is etched into a borofloat glass cover plate

Figure 2.4 illustrates the design of the first generation micro-CPL. The evaporator

plenum, the condenser plenum, and liquid/vapor lines are fabricated from a single crystal

silicon wafer. The wicking structure consists of axial grooves wet etched into a standard

borofloat glass wafer, which also serves as the cover plate. Glass was selected because of

its transparent nature, however the wicking structure will eventually be etched into the

backside of whichever electronic package requires cooling. A tube is connected to the

backside of the silicon wafer via a through hole in order to function as the reservoir feed

line. The working fluid enters an evacuated micro-CPL via this reservoir feed line, and

can only enter into the evaporator region through the axial grooves wet etched into the

glass cover plate. This wicking structure "pulls" the working fluid into the evaporator

region from the reservoir feed line by capillary forces, allowing for a wicking structure which can be re-wetted by the reservoir if necessary during operation. The heat supplied to the glass cover plate on the backside of these axial grooves in the evaporator region, creates the phase change which drives the capillary pumped loop. As explained in the beginning of this chapter, it is assumed that this heating results in an evaporative cooling mode within this wicking structure. In other words, a continuous liquid/vapor interface is assumed to exist along the entire length of these axial grooves, with the working fluid occupying the depth of the grooves covered on top by its vapor state. The phase change occurs with no bubbles being formed, therefore resulting in an assumed steady liquid/vapor interface with a distinct radius of curvature as previously illustrated. The pressure head gained from the radius of curvature of the vapor/liquid interface, and the pressure differential between the superheated vapor and subcooled liquid, drive the vapor along the vapor line towards the condenser. The vapor line is assumed to be adiabatic with no condensation, allowing for the vapor to travel all the way to the condenser. The vapor condenses within the condenser plenum, depositing the heat collected from the evaporator region. Here, an identical wicking structure is employed to draw the liquid from the condenser plenum into the liquid line, which is also assumed to be adiabatic. Liquid travels in this line, returning to the evaporator and re-entering the evaporator wicking structure from the side opposite of the reservoir feed line. The reservoir is off-chip and can be pressurized and/or heated, allowing for control of the operating temperature of the device.

II.3   Second Generation Sensitivity Analysis

A second generation micro-CPL was designed by selecting different evaporator and condenser sizes. The evaporator was enlarged to 1000 μm x 2000 μm, and the condenser was enlarged to an even greater area, 1250 μm x 2000 μm. Similar to the first generation design, fabrication limitations determined all other geometric parameters other than vapor/liquid line length. Table 2.4 shows the second generation micro-CPL specifications fixed prior to any sensitivity analysis.

Evaporator Length	2000 μm
Evaporator Width	1000 μm
Condenser Area	2.5e+06 sq. μm
Groove Height	55 μm
Groove Width	90 μm
Average Groove Radius	50 μm
Number of Grooves	8
Vapor Line Dimensions	150 x 340 μm
Liquid Line Dimensions	150 x 110 μm

Table 2.4 Specifications for the second generation micro-CPL

Similar to the first generation micro-CPL, a sensitivity analysis of total heat transport to liquid/vapor line length based on the capillary pumping limit was performed. Figure 2.5 shows the results of the sensitivity analysis in a graph of liquid/vapor line length vs. total heat transfer for the micro-CPL. A liquid/vapor line length of 35 mm corresponds to a maximum heat transfer rate of 4 W, and was selected as the vapor/liquid line length. Table 2.5 summarizes the final geometric parameters of the second generation micro-CPL, including Reynolds numbers and projected maximum heat transport.
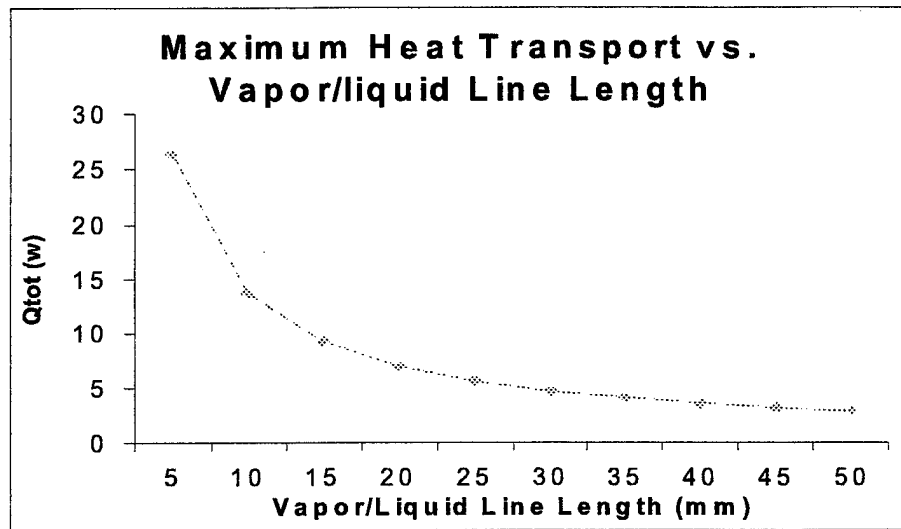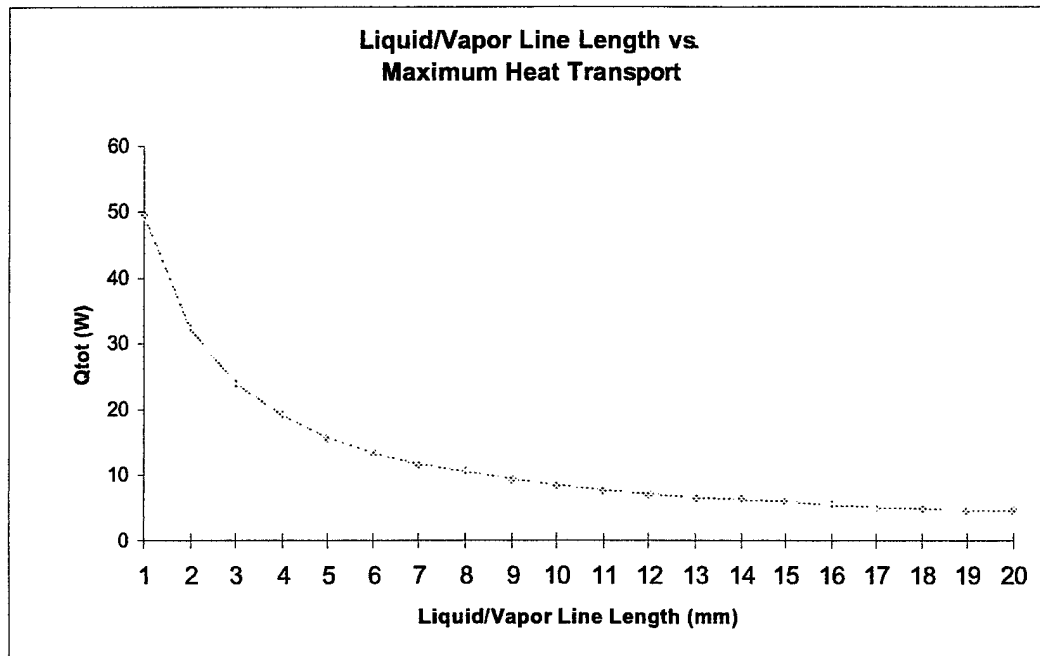
Figure 2.5 Maximum transport distance based on the capillary pumping limit for the second generation micro-CPL

Evaporator Length	2000 μm
Evaporator Width	1000 μm
Condenser Area	2.5e+06 sq. μm
Groove Height	55 μm
Groove Width	90 μm
Average Groove Radius	50 μm
Number of Grooves	8
Vapor Line Dimensions	150 x 340 μm
Liquid Line Dimensions	150 x 110 μm
Liquid Line Re Number	42
Vapor Line Re Number	488
Projected Heat Removal	4 Watts

Table 2.5 Parameters of the second generation micro-CPL

Figure 2.6 illustrates the design of the second generation micro-CPL which has

several distinct differences from the first generation design. The reservoir through-hole

25

now feeds both sides of the evaporator, as opposed to feeding only the one side opposite

of the liquid line. A second through-hole was also added to the condenser side of the

micro-CPL.

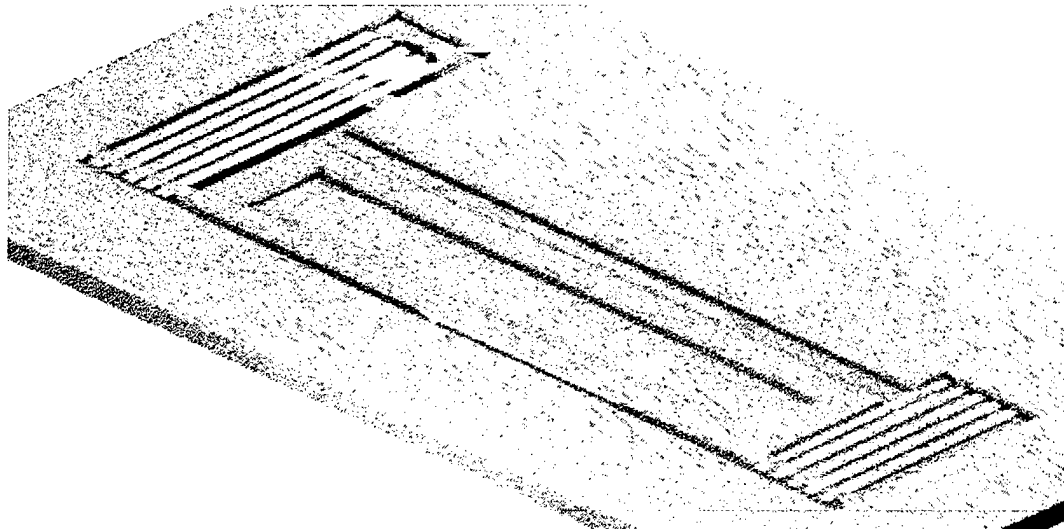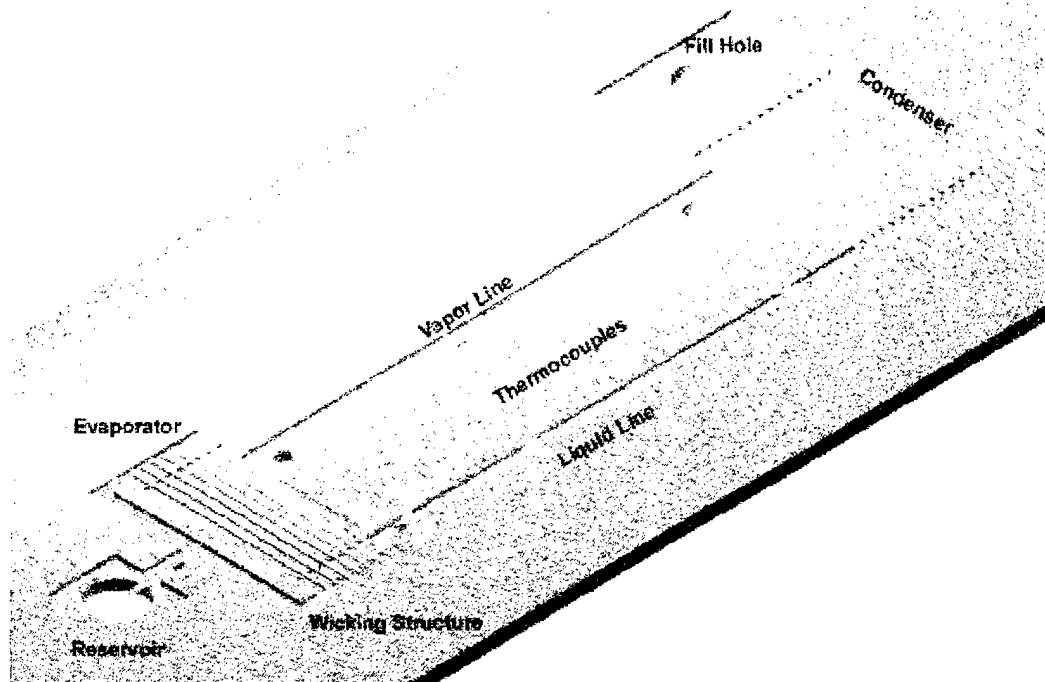**Figure 2.6 A sketch of the second generation micro-CPL. The fluidic channels (gray) are fabricated from silicon, while the wicking structure (white) is etched into a borofloat glass cover plate**

II.4 Wetting Angle Analysis of the Vapor Line

As explained more thoroughly in Chapter IV, there exists a vapor/liquid

condensation interface within the vapor line during start-up of the micro-CPL. It is

desirable that this interface move easily down the vapor line, with as little force "pulling"

the interface back towards the vapor as possible. and therefore the evaporator. Consider

the force diagram of the vapor/liquid interface within the vapor line shown in figure 2.7.
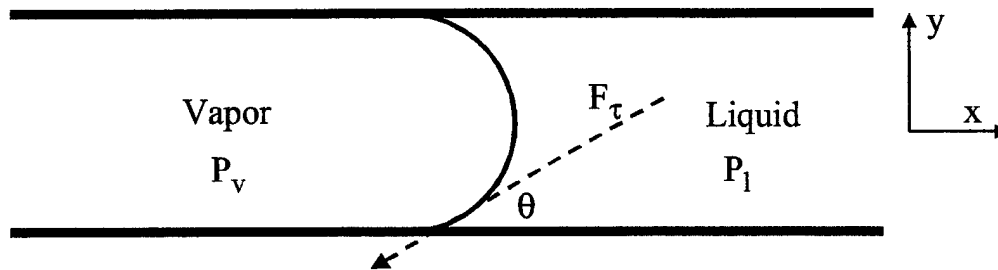
Figure 2.7 Force diagram on vapor/liquid interface within the vapor line

There are three distinct forces acting on the vapor/liquid interface. The pressure in

the vapor results in a force acting on the interface in the positive x-direction, and can be

expressed as

$$F_v = P_v A_I \qquad (2.19)$$

where A_I is the total area of the vapor/liquid interface. In a similar manner, the pressure in

the liquid results in a force acting on the interface in the negative x-direction, and is

expressed as

$$F_L = P_L A_I \qquad (2.20)$$

Finally, as illustrated in figure 2.7, the surface tension of the liquid acts in the direction of

the contact angle that the interface makes with the wall of the duct. The total magnitude

of this force, F_τ, is obtained by multiplying the surface tension of the liquid, τ, by the

length of the perimeter of the liquid/vapor interface, L_{per}

27

$$F_\tau = \tau L_{per} \qquad\qquad (2.21)$$

This force can be broken down into two components, a force normal to the wall and a

force parallel to the wall acting in the negative x-direction.

$$F_{\tau-x} = \tau L_{per} \cos\theta \qquad\qquad (2.22)$$

$$F_{\tau-y} = \tau L_{per} \sin\theta \qquad\qquad (2.23)$$

By balancing the forces in the x-direction acting upon this interface, the following

expression is obtained

$$P_v A_I = P_L A_I + \tau L_{per} \cos\theta \qquad\qquad (2.24)$$

In order to minimize the force acting in the negative x-direction, thereby allowing

the least resistance when moving the interface in the positive x-direction during start-up

of the device, it is desirable to have the interface be almost normal to the walls so that the

contact angle θ approaches 90 degrees. As explained in Chapter III, this was

accomplished by altering the free energy of the vapor line surface by coating the entire

micro-CPL with a 1H,1H,2H,2H-perfluoro-decyltrichlorosilane (FDTS) Self Assembled

Monolayer (SAM). This 2 nm thin, chain molecule coats both silicon and glass, and

increases water's contact angle to almost 90 degrees (Srinivasan, et. Al, 1997).

II.5 Two Dimensional Numerical Analysis

All temperature data for the micro-CPL was obtained from thermocouples placed along the backside of the silicon wafer. Interpretation of this data requires insight into the nature of the heat transfer within the materials comprising the micro-CPL, specifically glass and silicon.

The physical system of interest is shown in figure 2.8. Two wafers, one borofloat glass and the other of single crystal silicon, are anodically bonded and placed in a vertical position. Both wafers have a thickness of 5×10^{-4} m, and a radius of 0.05 m. A spot on the center of the glass wafer with a radius of 1.75 mm delivers a constant heat output of 8.5 W. The wafers are exposed to the ambient, with free convection occurring at the boundaries. Table 2.6 summarizes the parameters of interest.
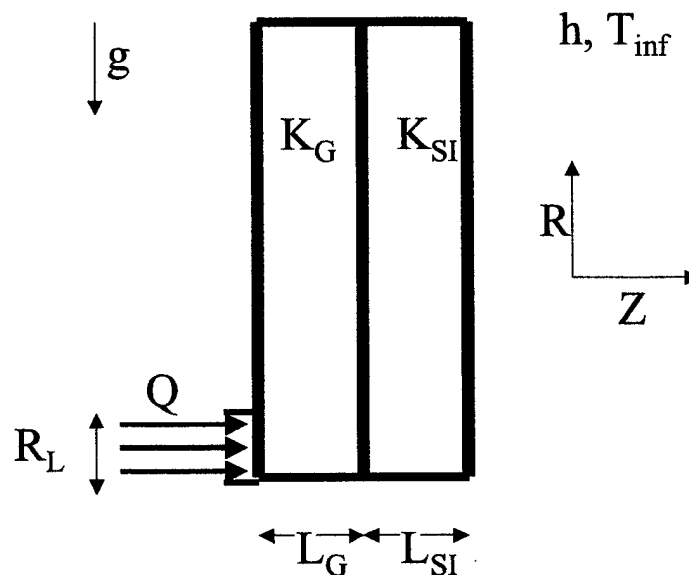
Figure 2.8 Physical set-up of the "Blank" Case

VARIABLE	DEFINITION	VALUE
D_L	Spot Size Diameter	3.5×10^{-3} m
L_G	Thickness of Glass Wafer	5.0×10^{-4} m
L_{SI}	Thickness of Silicon Wafer	5.0×10^{-4} m
Q	Heat Power Supplied over Spot	8.5 W
K_G	Glass Conductivity	1.4 W/m-K
K_{SI}	Silicon Conductivity	151 W/m-K

Table 2.6 Parameters used in the numerical simulation.

This multi-wafer system is modeled in cylindrical coordinates. The problem is assumed to have no angular dependence, and is symmetric in the radial coordinate, which is parallel to gravitational acceleration. Table 2.7 shows the well-posed mathematical problem. As illustrated in figure 2.7, the system can be represented as two half wafers extending from R = 0 to R = 0.05 m, which is the outer radius of the wafers. The longitudinal coordinate extends from Z = 0 to Z = 1.0×10^{-3} m, which is the sum of the thickness of both wafers. The origin of the coordinate system is placed at the center of the laser dot. During steady-state, Laplace's equation governs the heat transfer within the wafers.

Governing Equation	Range	Comments
$\nabla^2 T = 0$	$0 < R < 0.05$ m $0 < Z < 5.0\text{x}10^{-4}$ m	Steady State Heat Equation
$\nabla^2 T = 0$	$0 < R < 0.05$ m $5.0\text{x}10^{-4}$ m $< Z < 1.0\text{x}10^{-3}$ m	Steady State Heat Equation
$-k_g \dfrac{\partial T}{\partial Z} = 8.83\text{x}10^5 \dfrac{W}{m^2}$	$0 < R < 1.75\text{x}10^{-3}$ m, $Z = 0$	Laser Flux B.C.
$-k_g \dfrac{\partial T}{\partial Z} = h(T - T_{inf})$	$1.75\text{x}10^{-3}$ m $< R < 0.05$ m, $Z = 0$	Natural Convection B.C.
$k_g \dfrac{\partial T}{\partial Z_<} = k_{si} \dfrac{\partial T}{\partial Z_>}$ $T_< = T_>$	$0 < R < 0.05$ m, $Z = 5.0\text{x}10^{-4}$ m	Composite Material B.C.
$-k_{si} \dfrac{\partial T}{\partial Z} = h(T - T_{inf})$	$0 < R < 0.05$ m, $Z = 1.0\text{x}10^{-3}$ m	Natural Convection B.C.
$-k_g \dfrac{\partial T}{\partial R} = h(T - T_{inf})$	$R = 0.05$ m, $0 < Z < 5.0\text{x}10^{-4}$ m	Natural Convection B.C.
$-k_{si} \dfrac{\partial T}{\partial R} = h(T - T_{inf})$	$R = 0.05$ m, $5.0\text{x}10^{-4}$ m $< Z < 1.0\text{x}10^{-3}$ m	Natural Convection B.C.
$\dfrac{\partial T}{\partial Z} = 0$	$R = 0, 0 < Z < 1.0\text{x}10^{-3}$ m	Adiabatic (Symmetry)

Table 2.7 Mathematical description of numerical model

It is first necessary to evaluate the natural convection coefficient h, which shall be assumed constant for this problem. For free convection on a vertical surface, the first step is to determine the Grashof number, which is the ratio buoyancy to viscous forces.

$$Gr = \frac{g\beta(T_s - T_{inf})L^3}{v^2}$$ (2.25)

Here g is the acceleration due to gravity, β is $1/T_{gas}$ for an ideal gas, T_s is the surface temperature, L is the vertical length scale of interest, and v is the kinematic viscosity (Incropera and DeWitt, 1981, p. 487).

The area on the front side of the glass which is being heated has a spot diameter equal to D_L, so $L = D_L = 3.5 \times 10^{-3}$ m. The backside temperature of the silicon is assumed to be on the order of 100 C, so $T_s = 373$ K, while $T_{inf} = 293$ K. Assuming that the air surrounding the heated area will be at a temperature less than T_s, but greater than T_{inf}, T_{gas} is approximated as an average of T_s and T_{inf}. Therefore $T_{gas} = 333$ K, $\beta = 1/333$ K, and the Grashof number is

$$Gr = \frac{(9.8)\left(\frac{1}{333}\right)(373 - 293)(0.0035)^3}{(16x10^{-6})^2} = 394$$

The Prandtl number, which is the ratio of momentum and thermal diffusivities, is $Pr = v/\alpha = 0.7$ (Incorpera and DeWitt, 1981, p. 312). Therefore $GrPr = (394)(0.7) = 276$, and it was determined that $Nu = 3.16$ (Incorpera and DeWitt, 1981, p. 493).

32

Finally, using $L = 3.5\text{x}10^{-3}$ m, and $k_{air} = 30 \text{ x } 10^{-3}$ W/m-K, $h = 27$ W/m^2-K.

A two-dimensional axis-symmetric numerical model of figure 2.8 was created using the CFD-ACE code developed by CFDRC (Computational Fluid Dynamics Research Corporation). The geometry was modeled using a grid with 20 nodes in the Z direction, and 200 nodes in the R direction. "CFD-ACE employs a cell-centered control volume approach [with four sided cells in two-dimensions]. This approach implies that the discrete equations are formulated by evaluating and integrating the fluxes across the faces that surround each control volume." (CFDRC, 1998) The temperature profile generated is shown in figure 2.9. It should be noted that due to the model's axial-symmetry, the bottom of the figure is actually the center of the wafers where the heat is being supplied on the left side, and the wafers extend radially upward a distance of 20 mm. The top of the figure has been truncated in order to show the area of interest in more detail.
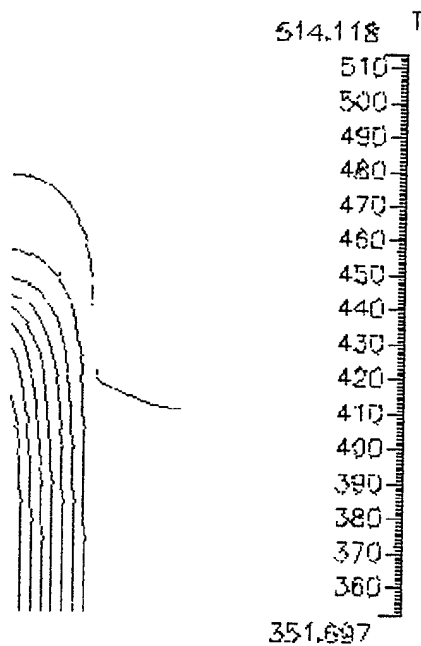
Figure 2.9 Temperature profile generated by the 2-D axis-symmetric numerical model

Although no specific quantitative information shall be used from this model, a

general qualitative conclusion can be drawn. While the wafers are supporting a

temperature gradient in both directions on the order of 150 K, these gradients exist

primarily in the glass wafer on the left. Therefore, it seems reasonable to use the backside

thermocouple temperature readings presented in Chapter V as the temperature that exists

at the glass/silicon junction.

34

Chapter III. Fabrication

III.1 Construction of the Fluidic Channels In Silicon

In order to maintain chip-level temperature control, the fabrication of a micro-CPL must be compatible with the fabrication of the electronic package to be cooled. One of the major advantages to utilizing MEMS technologies in micro-CPL fabrication, is that it allows for both the electronic package and micro-CPL to be created in the same environment, thereby allowing from complete integration of the micro-CPL into the electronic element for more efficient thermal management.

Apart from the wicking structure, the entire micro-CPL is fabricated from silicon. Silicon was selected not only because of its compatibility with electronic packaging, but because of the fabrication requirements of the micro-CPL. The liquid and vapor lines require straight sidewalls with significantly large depths (150 μm). Silicon is ideal for this purpose, as Deep Reactive Ion Etching (DRIE) allows for straight vertical surfaces. Specifically, a Surface Technology Systems (STS) DRIE was used, which utilizes an advanced silicon etch process consisting of alternating cycles of etching (SF_6) and protective polymer deposition (C_4F_8) to achieve the high aspect ratios desired. First, the silicon is coated with C_4F_8 which coats both the sidewalls and bottom of the channels being created. Then the SF_6, which is used in the etch step, etches through the C_4F_8 on the bottom of the trench, as well as the silicon underneath the protective polymer, yet it does

35

not etch through the C_4F_8 previously deposited on the sidewalls. The etch step is then stopped, and more C_4F_8 is deposited on the silicon. In this manner, the sidewalls of the silicon trenches are always protected, and only the bottom of the trench is etched, guaranteeing straight sidewalls.

The fabrication of the fluidic channels requires two distinct etch depths on a double-polished single crystal <100> silicon wafer. The first goes through the entire wafer and functions not only as the reservoir feed line, but also as the fill line prior to operation. The second etch is 150 µm deep, and creates the vapor/liquid lines, in addition to the evaporator and condenser plenums.

The materials used as sacrificial mask layers for the two deep etches are determined by the nature of the STS. Potential contamination of the STS process chamber allows for few masking layer options. The choices are photoresist, oxide, nitride and/or aluminum. One mask layer is deposited and patterned, and then a second mask layer is deposited and patterned on top of the first. This top mask layer, the one created last, is used for the first etch. Upon completion, this top mask is removed, revealing the other mask beneath it. It is therefore necessary to use separate materials for the two masking layers, or the removal of the first mask will lead to the removal of the second mask. Furthermore, the shallowest etch will be 150 µm deep, which is quite substantial. Aluminum is only useful for very shallow etches, because the metal has been observed to re-sputter on the open areas of the wafer if etched excessively in the STS. Finally, the poor selectivity of nitride leads to the selection of oxide and photoresist as the two masking layers.

Initially, 3 μm of oxide were thermally deposited onto a silicon wafer. This has

the added benefit of protecting the backside of the wafer from undercutting in the STS. A

photoresist mask was then created on top of the oxide. The oxide was plasma etched in a

Lam etcher in order to create the oxide mask for the fluidic channels. 8 μm of thick

photoresist (microposit 452) were then spun on top of the oxide mask, which once

exposed, developed and baked, served as a mask for the through holes. The wafer was

then placed into the STS, and the through-holes were etched. Once completed, the

remaining photoresist was stripped thus revealing the oxide mask beneath it. The wafer

was then deep trench etched 150 μm, creating the fluidic channels. This process is

outlined in figure 3.1, and pictures of the silicon after processing are in figure 3.2.

1) Thermal Oxide Deposition (3 μm)

2) Photolithography

3) Plasma Etch to Pattern Oxide Layer

4) Second Photolithography

5) DRIE (Deep Reactive Ion Etching) of Through-hole

6) Second DRIE to create fluidic channels
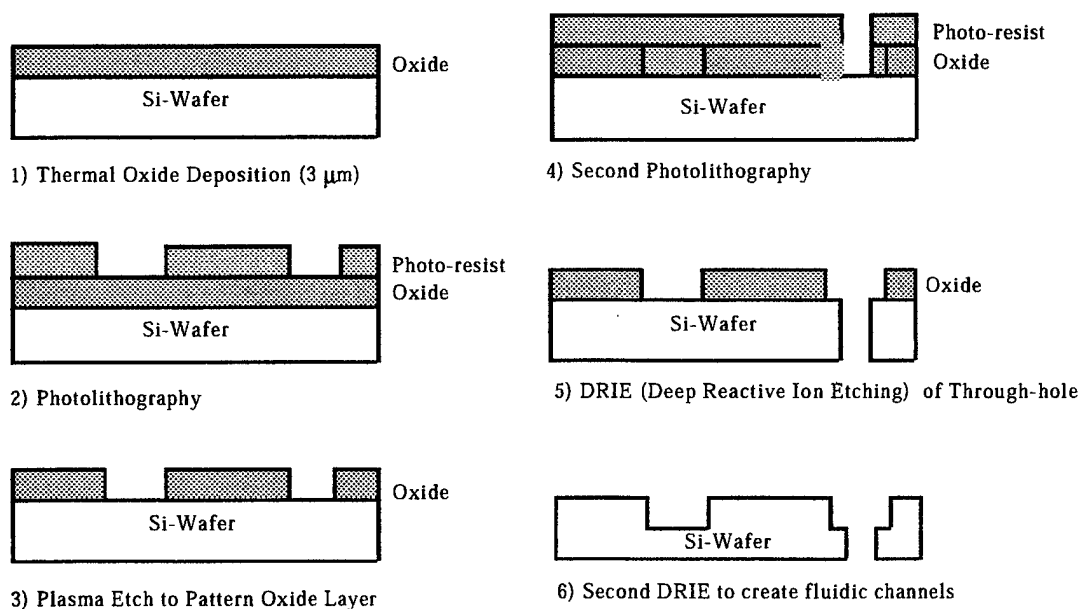
Figure 3.1. Fabrication process for the silicon wafer
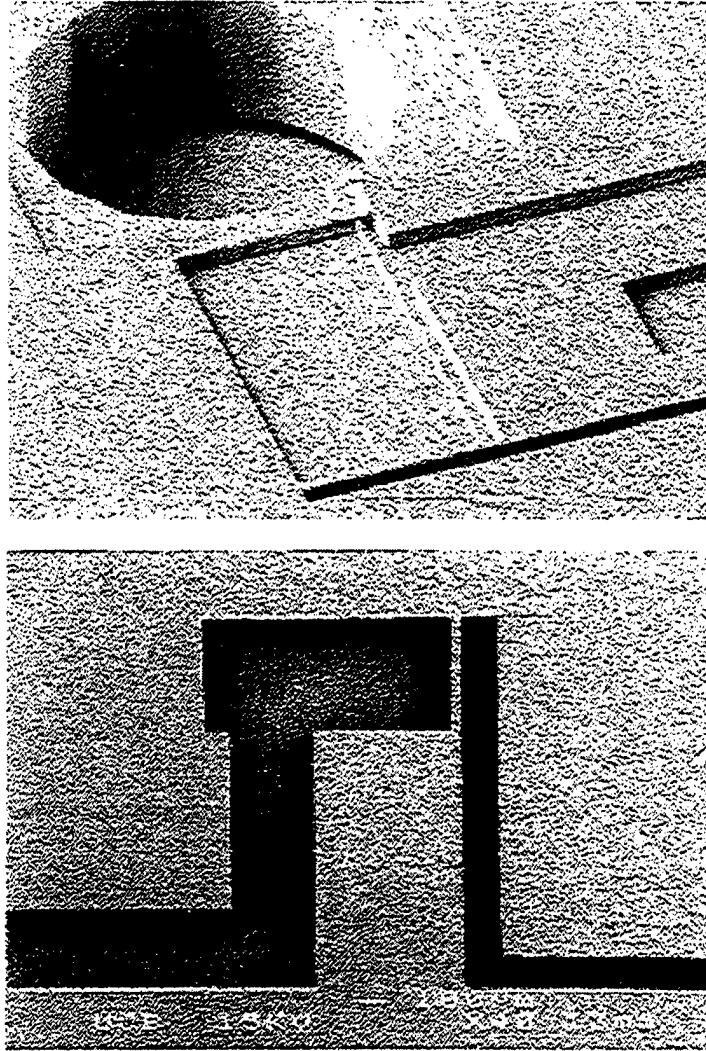
Figure 3.2 (a) The evaporator and (b) condenser fabricated from silicon

III.2   Construction of the Wicking Structure in Glass

While the wick structure for the micro-CPL will eventually be fabricated directly

into the electronic package requiring cooling, glass was used for flow visualization

during experimentation. Although glass's transparent nature is ideal for the initial

experiments, it also has distinct fabrication limitations. While DRIE can be used on silicon to create straight sidewalls, this was not an option for the glass wafer. The wick structure was etched from the glass using an isotropic wet etch, essentially placing the glass into an acid. Since the concentrated Hydroflouric (HF) acid will etch glass equally in all directions, the axial grooves in the glass are hemispherical, as explained in Chapter II. Furthermore, immersion of the entire glass wafer into the acid requires that the backside of the wafer be protected from unwanted etching. The need to pattern the front of the glass wafer (to create the axial grooves), coupled with the need to protect the backside of the glass, led to the selection of polysilicon as the masking layer.

1 μm of undoped polysilicon was deposited on the glass wafer at 823 K. This lower temperature avoids even the slightest melting of the burofloat glass, which can make the surface too rough for anodic bonding. A photoresist mask was used when placing the wafer in CF_4 plasma. After stripping the photoresist, but prior to the wet etch, standard disco tape (120 μm thick) was placed on the backside of the wafer to help further protect it during the wet etch. The wafer was then placed in concentrated hydrofluoric acid for 6 minutes, completing the creation of the 50 μm deep axial grooves which function as the micro-CPL wicking structure. This process is outlined in figure 3.3, and pictures of the wick structure after processing are shown in figure 3.4.

1) Undoped Polysilicon Deposition (1.0 μm)

2) Photolithography

3) Plasma etch of Polysilicon

4) Wet Etch using Concentrated HF
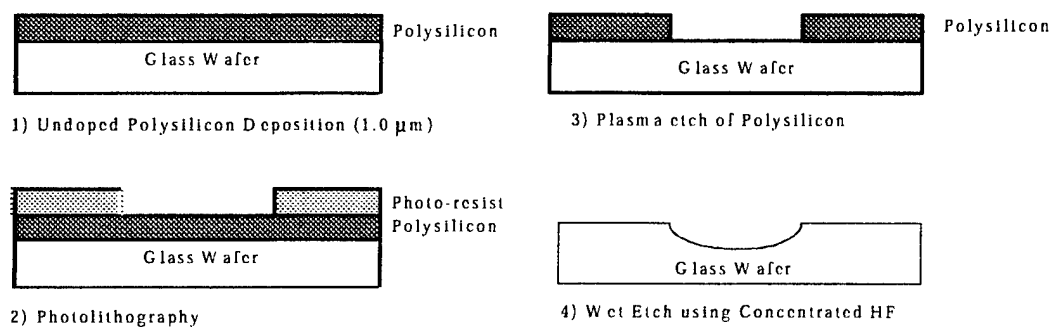
Figure 3.3 Fabrication process for the glass wafer
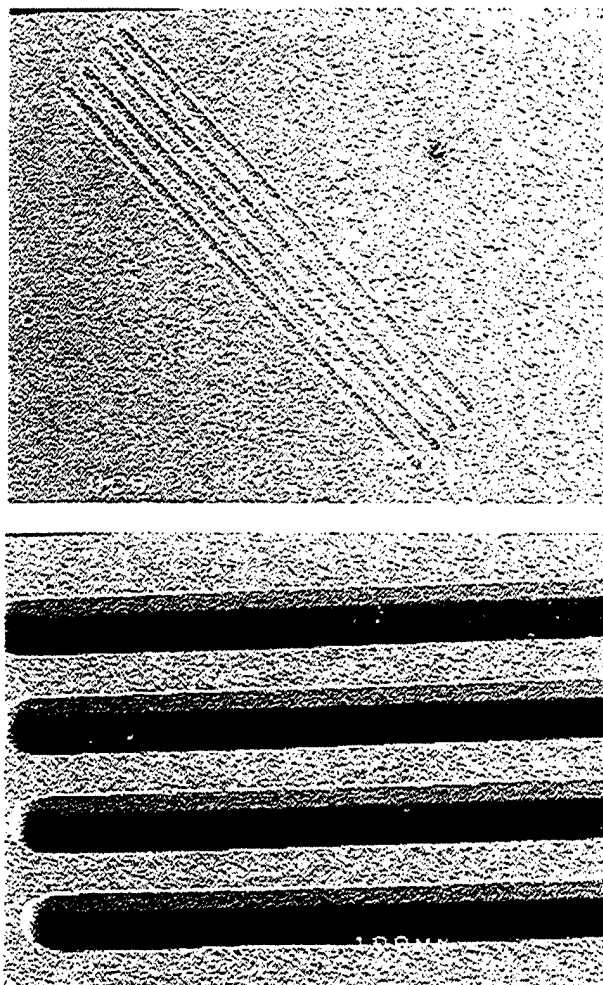
Figure 3.4 (a) Picture of the wick structure in glass and (b) upclose view.

Finally, it is necessary to bond the fluidic channels in the silicon to the wicking structure in the borofloat glass wafer. After aligning the two wafers, field-assisted thermal bonding, also known as anodic bonding, was used. The two wafers are heated to 450 C, and a voltage drop of 1500 V is applied across them for an hour. Although the anodic bonding mechanism is not fully understood, it is believed that the dominant mechanism is the migration of sodium ions in the borofloat glass towards the silicon. This migration leaves spare negative charges in the region of the glass-silicon interface, which results in covalent bonds forming between the glass and silicon (Madou, 1997).

III.3 Hydrophobic Coating of the Micro-CPL

As explained in Chapter II, it is desirable to coat the micro-CPL such that the vapor line, evaporator plenum and condenser plenum are hydrophobic. This was achieved by coating the entire micro-CPL with a Self Assembled Monolayer (SAM). Specifically, 1H,1H,2H,2H-perfluorodecyltrichlorosilane (FDTS) SAM was chosen because anodic bonding requires temperatures of at least 623 K, which the FDTS SAM has been proven to survive at. This 2 nm thin, chain molecule coats both silicon and glass, and has the effect of altering the coated surface's free energy, thereby changing water's contact angle with the material. (Srinivasan et al., 1997) A detailed outline of the complete fabrication of the micro-CPL can be found in Appendix B.

Chapter IV. Experimental Method

IV.1 Experimental Set-Up

In order to acquire data about the micro-CPL's heat transfer performance, the following experimental apparatus was constructed. The center of two anodically bonded wafers were mounted to a dial on the silicon side, which controls the angular orientation of the micro-CPL fabricated within these wafers. A Becton Disckinson 20G1 needle was fastened in the micro-CPL's through hole with Varian's vacuum epoxy, and was attached to a two-way valve. This valve connects the micro-CPL to either a roughing/turbo pump configuration, or the working fluid reservoir. The reservoir is also connected to a supply of compressed air, to allow for control over the reservoir's operating pressure. Three type E nickel/chromium-constantan Omega thermocouples were then placed on the backside of the silicon wafer. Temperature data were recorded using standard data acquisition software. A CO_2 laser was used to heat the glass side of the evaporator region, and was focused in place with the aid of a HeNe targeting laser. A lens placed in the path of the CO_2 laser controlled the spot size diameter heating the glass wafer. A beam splitter allowed for laser output calibration with a power sensor. Finally, a digital camera recorded pictures of the micro-CPL during operation. A schematic of the experiment is illustrated in figure 4.1, and a picture of the apparatus is displayed in figure 4.2.
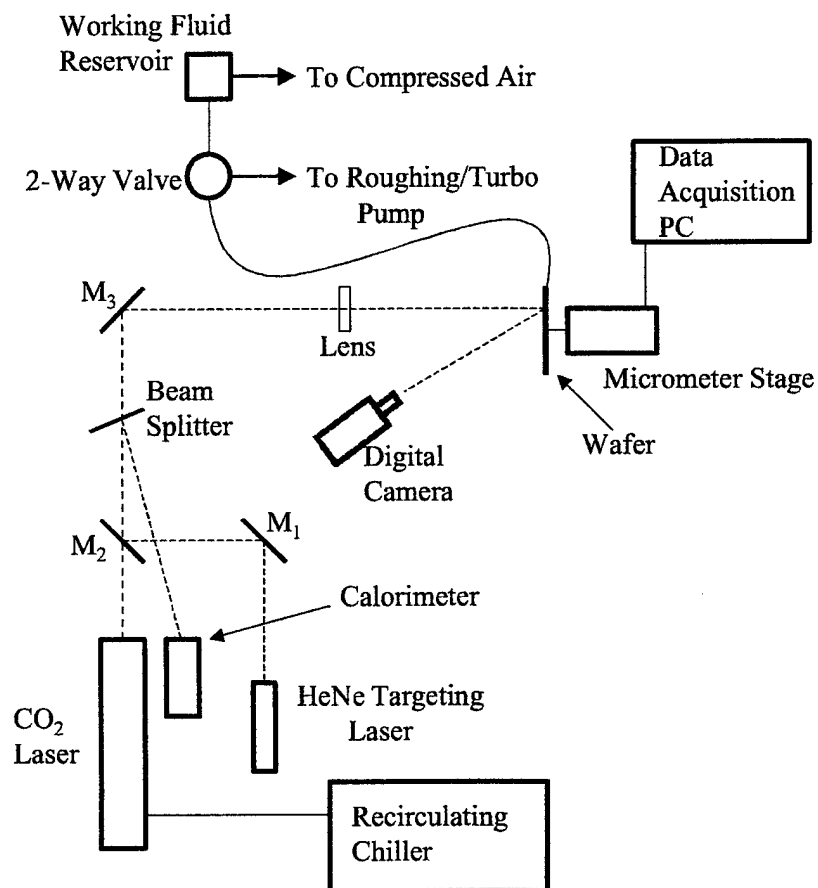
Figure 4.1 Schematic of experimental set-up
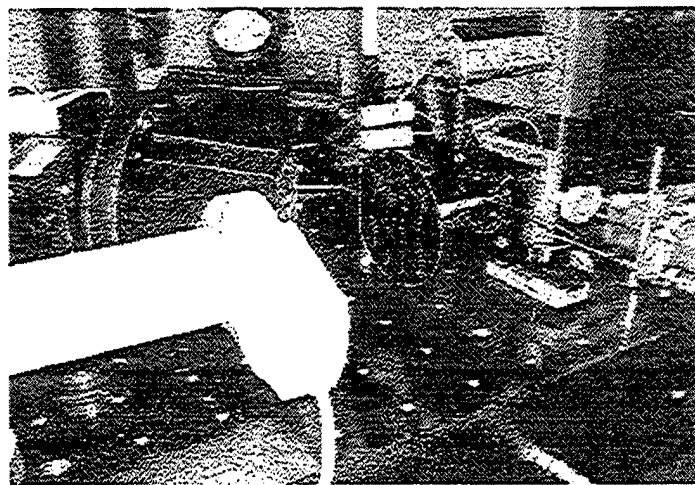
Figure 4.2 Picture of experimental set-up

43

IV.2 Experimental Procedure

Utilizing this apparatus, several experiments were conducted to obtain insight into the heat transfer characteristics of the micro-CPL. Different wafer configurations were tested, some with first generation micro-CPL designs, some with second generation designs, and some with no micro-CPL present at all. Different power output and spot size diameters of the CO_2 laser were used to power a micro-CPL. The device was tested in both horizontal and vertical orientations, utilizing ethanol, water or air as the working fluid. Finally, a hydrophobic micro-CPL, which had been coated with FDTS SAM was also studied. A list of all the experiments conducted is reprinted in table 4.1.

Micro-CPL Design	Heat Source	Spot Size Diameter	Power Output	Orientation	Working Fluid	Hydrophobic Coating	Res. Pressure
First Generation	Micro-torch	Unknown	Unknown	Horizontal	Ethanol	No	15 psi
First Generation	Micro-torch	Unknown	Unknown	Horizontal	Water	No	15 psi
Second Generation	CO_2 Laser	3.5 mm	8.5 W (+/- 0.2 W)	Horizontal	Water	No	15 psi
Second Generation	CO_2 Laser	3.5 mm	8.5 W (+/- 0.2 W)	Vertical	Water	No	15 psi
None – Blank Wafers	CO_2 Laser	1.0 mm	7.5 W (+/- 0.2 W)	N/A	N/A	N/A	N/A
Second Generation	CO_2 Laser	1.0 mm	7.5 W (+/- 0.2 W)	Horizontal	Air	No	Amb
Second Generation	CO_2 Laser	1.0 mm	7.5 W (+/- 0.2 W)	Horizontal	Water	No	15 psi
Second Generation	CO_2 Laser	1.0 mm	7.5 W (+/- 0.2 W)	Horizontal	Water	Yes	15 psi

Table 4.1 List of the test configurations

44

The first set of experiments were qualitative in nature, and confirmed the design validity of the first generation micro-CPL. The device was made to run near steady state by supplying heat to the evaporator region with a hand-held micro torch. The exact amount of heat supplied was unknown, and the flame size was significantly larger than the evaporator. The working fluid's reservoir was pressurized to 15 psi above ambient. Both ethanol and water were used as the working fluid.

The next set of experiments were performed on the second generation micro-CPL with controlled heating by a CO_2 laser. The micro-CPL was tested in both the vertical (reflux mode) and horizontal orientations, by adjusting the angular orientation of the wafer configuration. A laser power output of 8.5 W (+/- 0.2 W) was delivered to the evaporator region with a laser spot size diameter of 3.5 mm, which was still larger than the 1000 μm x 2000 μm evaporator. Water was used as the working fluid, and the reservoir was pressurized to 15 psi above ambient. Thermocouples were placed on the backside of the evaporator, condenser and liquid line. Figure 4.3 shows the wafer configuration during testing, and illustrates the thermocouple locations.
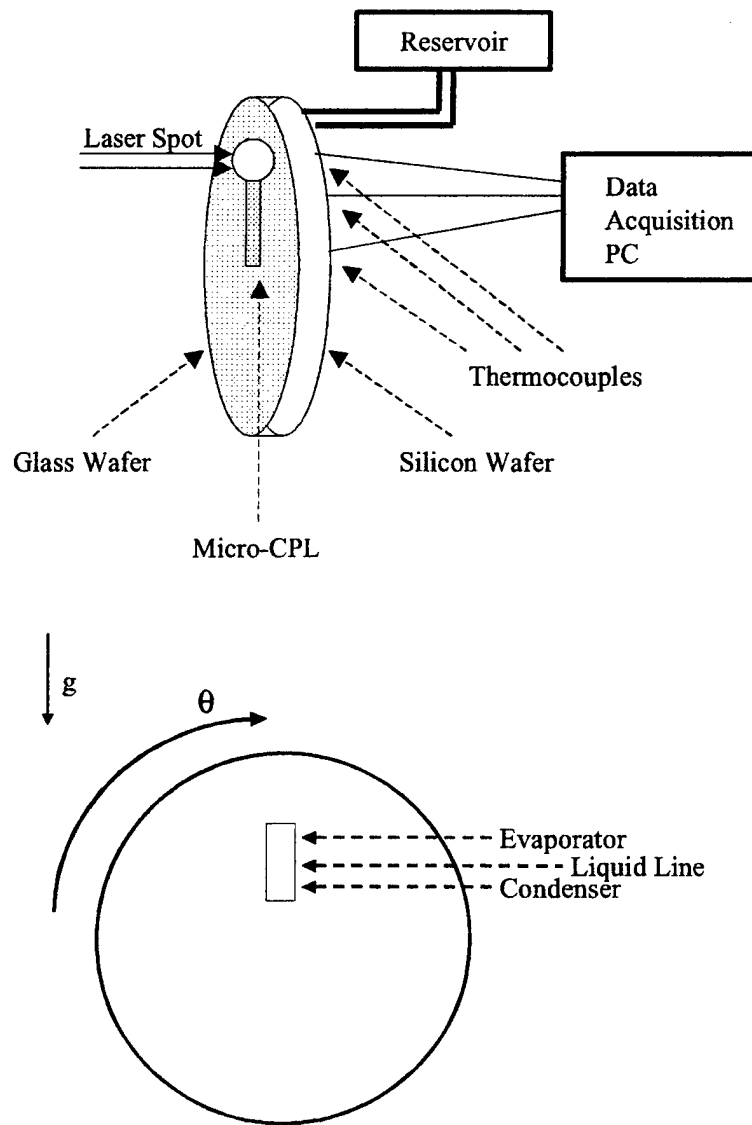
Figure 4.3 (a) Side and (b) Front view of experiments with 8.5 W (+/- 0.2 W) laser spot heating

In the third set of experiments, the heat supplied by the CO_2 laser was delivered to the backside of the micro-CPL's wick structure. The laser delivered a power output of 7.5 W (+/- 0.2 W) over a spot size diameter of 1.0 mm. The device was operated with water

as the working fluid, with the reservoir pressurized to 15 psi above ambient. The micro-CPL was also operated with air as the working fluid, by not attaching the through-hole to a reservoir. A micro-CPL coated with the FDTS SAM hydrophobic coating with water as the working fluid was also tested. Thermocouples were placed in the identical positioning as the previous experiments, with the noted exception that the liquid line thermocouple was moved to the backside of the center of the vapor line. Finally, a blank set of identical wafers (one glass and one silicon, both with 100 mm diameter with 500 µm thickness) were also tested with this laser output and spot size. In this case, the laser spot was focused on the glass wafer at a point 20 mm away from the edge of the wafer, and 30 mm away from the center of the wafer. This location mimics the location where the micro-CPL's evaporator region lies when devices are fabricated into similar wafers. The remaining thermocouples were placed at distances of 19 mm and 45 mm away from the center of the wafers along the same line as the first thermocouple, and are referred to as "Inboard" and "Outboard" respectively. Side and front views of this "Blank" set-up are shown in figure 4.4.
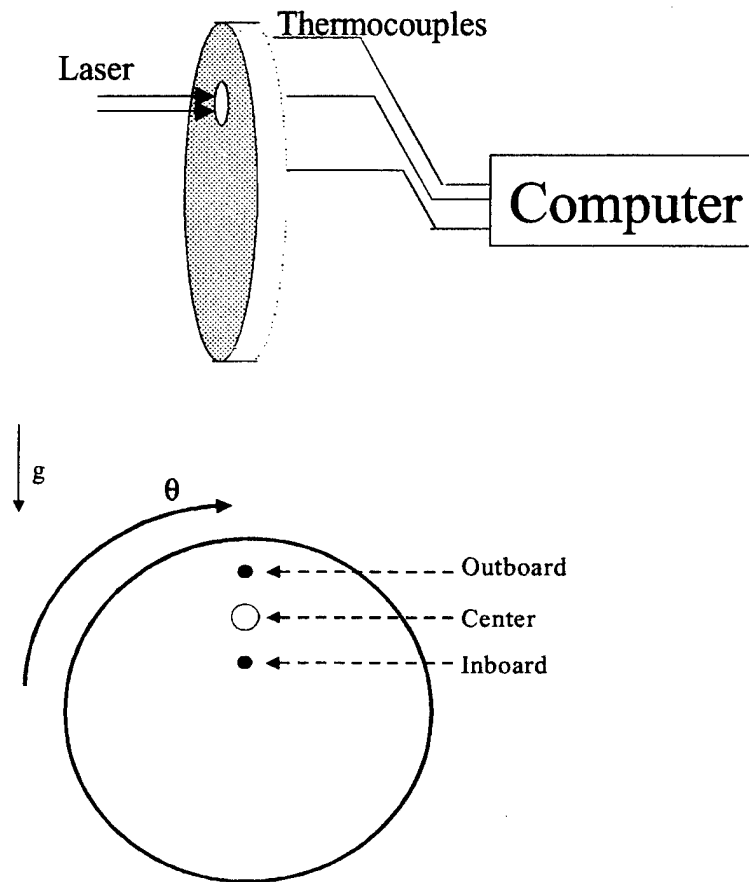
Figure 4.4 (a) Front view and (b) Side view of the "Blank" case experiment

Initial preparation of the micro-CPL mirrors that of larger, traditional CPLs. Apart from the blank wafer experiment, and the device which utilized air as its working fluid, the micro-CPL needed to be "filled" prior to operation. A roughing/turbo pump configuration was used to evacuate all air from the device, in order to avoid vapor-lock during operation. Then, just as with traditional CPLs, the entire device is flooded with the working fluid. It was at this point that the reservoir was pressurized to 15 psi above ambient. Finally, a hand-held micro-torch was used to heat to the vapor line before heat was supplied to the evaporator region. The heating of the vapor line begins evaporation, and is continued until the vapor line is "cleared-out." While the "clearing-out" of the

48

vapor line is not absolutely necessary, as the micro-CPL can be started by simply heating the evaporator after filling, it is done to enhance the device's performance during start-up. As with traditional CPLs, when heat is supplied to the evaporator region of a completely filled device, phase change will begin in the evaporator plenum. As predicted by the Clausius-Clapeyron equation (2.10), the superheated vapor forming in the evaporator region will eventually become hot enough, compared to the liquid in the vapor line, and develop a large enough pressure difference to clear-out the vapor line. Once the vapor line is "cleared-out", the temperature of the superheated vapor in the evaporator region will drop back down to just above the saturation temperature of the working fluid. In order to avoid this temperature spike during start-up, the vapor line of the micro-CPL was "cleared-out" prior to operation.

Chapter V. Results and Discussion

V.1   Qualitative Experiments

Initial experiments preformed on the micro-CPL confirmed the validity of the

design, while highlighting several parameters inhibiting the device's overall performance.

Recall that the first experiments were solely qualitative, utilizing a hand-held micro-torch

to heat the evaporator of the first generation design. There was no active cooling

mechanism used on the condenser other than natural convection, and the entire device

was exposed to the ambient with no insulation. The micro-CPL operated with ethanol and

water as its working fluid, and the pressure in the reservoir varied between 10 and 30 psi

above ambient. The geometric parameters and design of the first generation micro-CPL

are reprinted in table 5.1 and figure 5.1. Pictures of the evaporator and condenser regions

during steady-state operation are shown in figures 5.3 and 5.4 respectively.

Evaporator Length	1000 μm
Evaporator Width	500 μm
Condenser Area	5.0e+05 sq. μm
Groove Height	55 μm
Groove Width	90 μm
Average Groove Radius	50 μm
Number of Grooves	4
Vapor Line Dimensions	150 x 450 μm
Liquid Line Dimensions	150 x 150 μm
Vapor/Liquid Line Length	35 mm

Table 5.1 Parameters of the first generation micro-CPL
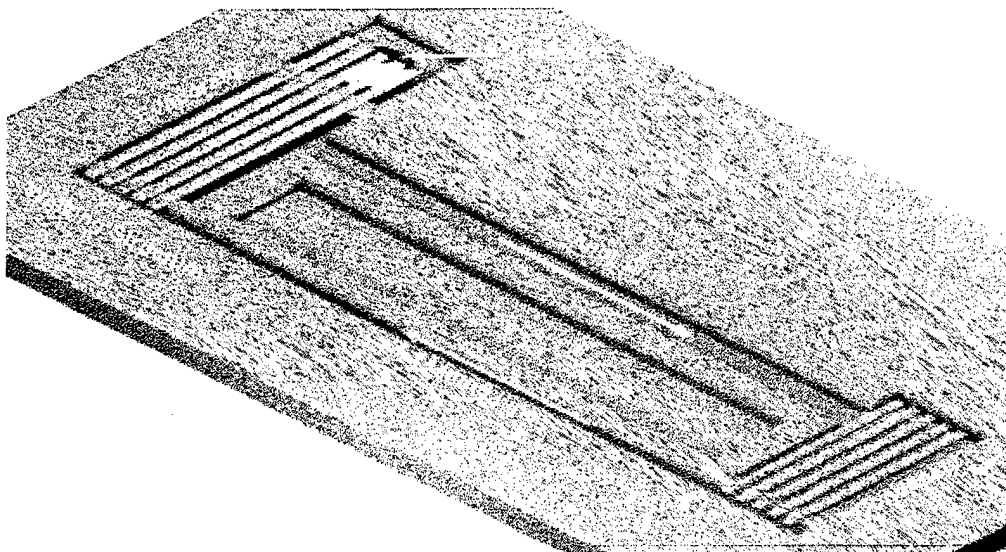
Figure 5.1 A sketch of the micro-CPL. The fluidic channels (gray) are fabricated from silicon, while the wicking structure (white) is etched into a borofloat glass cover plate
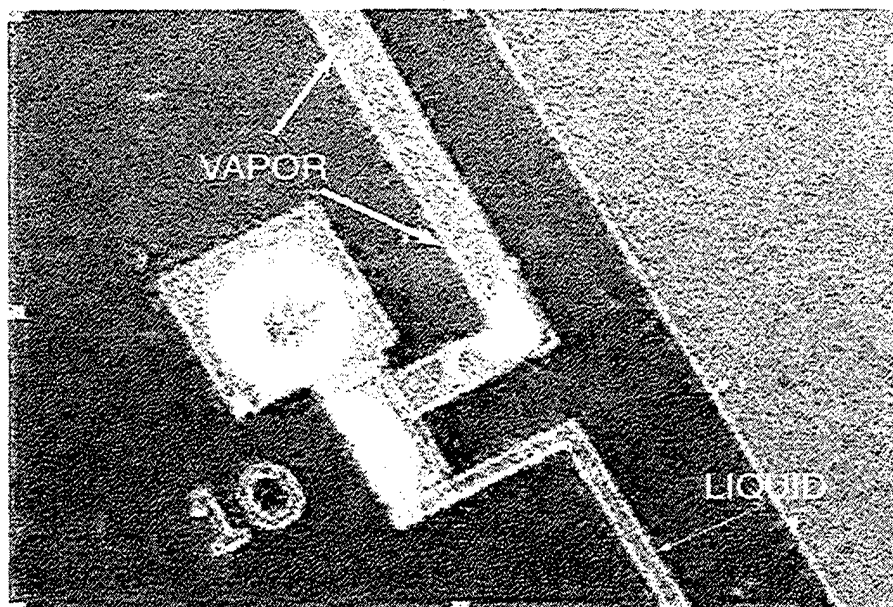
Figure 5.2 Evaporator region during the initial experiment
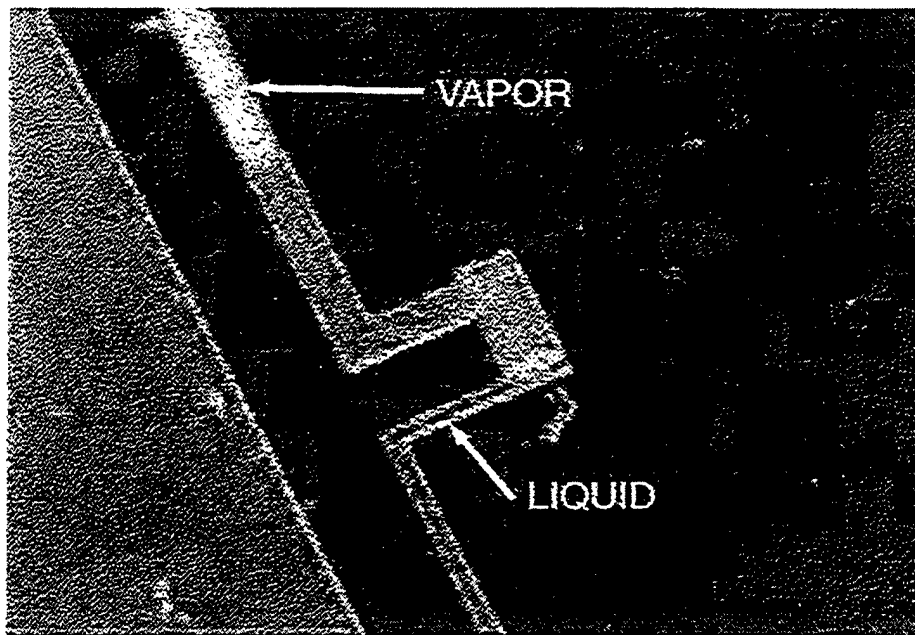
Figure 5.3 Condenser region during the initial experiment

Prior to operation, the difficulty encountered in evacuating the micro-CPL

revealed the first shortcoming of this preliminary design. With only one through-hole in

the silicon, evacuating the entire device, including its 35mm vapor/liquid lines, was

extremely difficult. While the combination of a roughing/turbo pump was finally

successful, it became apparent that adding a second through-hole to the condenser side of

the device would immediately solve this problem.

The micro-CPL's small length scales, and resulting large surface area to volume

ratios, have a direct impact on micro-CPL performance. After filling and pressurizing the

device, the vapor line was cleared out with the micro-torch to aid in start-up. The

backside of the micro-CPL was exposed to the ambient, and the large surface area to

volume ratio in the vapor line allowed for heat to be removed from the superheated

vapor, transported through the wafers, and convected off to the ambient. This non-adiabatic nature of the vapor line, which is in direct contrast to the assumption made in the capillary pumping limit analysis in Chapter II, resulted in early condensation in the vapor line. The vapor/liquid condensation interface, which was at the condenser region when the vapor line was cleared with the hand torch, was observed to recede up the vapor line towards the evaporator region. In order to prevent this from occurring, the micro-torch would occasionally be applied over the vapor line, essentially replacing the heat being lost from backside convection. Figure 5.3 shows the vapor/liquid condensation interface remaining near the condenser when the vapor line was kept isothermal in this manner.

It is also readily apparent from figure 5.2 that the final liquid/vapor evaporation interface is actually in the vapor line, and not in the evaporator plenum. This is attributed to the large flame size of the micro-torch, which is significantly greater than the 500 μm x 1000 μm evaporator, and highlights the need to confine the heating to the backside of the evaporator's wick structure.

Further examination of Figure 5.2 directs attention to a problem existing at the liquid line/evaporator region interface. Vapor is observed at the end of the liquid line, obstructing part of the inlet to the evaporator, resulting in a substantially lower liquid return from the line to the evaporator wicking structure. This partially "dried-out" wicking structure results in a lower operational mass flow rate. In order to supply more liquid to the wicking structure, and thereby increase the total heat transport of the device, it would be beneficial to have the reservoir feeding both sides of the evaporator.

Another interesting observation about the micro-CPL centered around the modes of operation in the evaporator wick structure. Unlike traditional CPLs, the micro-CPL evaporator only has two modes of operation. Initially there is no phase change occurring, and the evaporator is "removing heat" by taking advantage of the sensible heating of the fluid. Once phase change starts, the evaporator immediately operates in the nucleate boiling mode. This is in direct contrast with the multiple modes which have been observed in traditional CPLs, and has specific implications towards the capillary pumping limit theory presented in Chapter II. The equation for pressure drop across the wicking structure (2.13) assumes the evaporator is operating in an evaporative cooling mode with no boiling. While the boiling in the evaporator wicking structure did not result in device failure, the pressure drop across the wicking structure needs to be remodeled to take into account the increased pressure drop that the bubbles create within the axial grooves.

Finally, and perhaps most obvious, the issue of condenser size needed to be addressed. In this first version of the micro-CPL, the condenser and evaporator regions were the same size. The purpose of the micro-CPL is to target moderate to large heat fluxes, and move the heat to a larger area where more traditional methods of thermal management can be utilized. If the condenser region deposits heat fluxes too large to remove, then the condenser limit discussed in Chapter I will be encountered. Future micro-CPL designs will have condensers which are larger than their evaporators, which will serve to spread and lower the heat fluxes.

These qualitative observations led to a re-design of the micro-CPL. The evaporator was enlarged to 1000 μm x 2000 μm, and the condenser was enlarged to an

even greater area, 1250 μm x 2000 μm. The average radius of the axial grooved wicking

structure remained 50 μm, so the larger evaporator width allows for eight grooves,

instead of the previous four The reservoir through-hole now feeds both sides of the

evaporator. Finally, a second through-hole was also added to the condenser side to aid in

filling. Figure 5.4 is a re-print of the second generation design of the micro-CPL which

has incorporated these new feature, while table 5.2 lists the geometric parameters of the

new design.
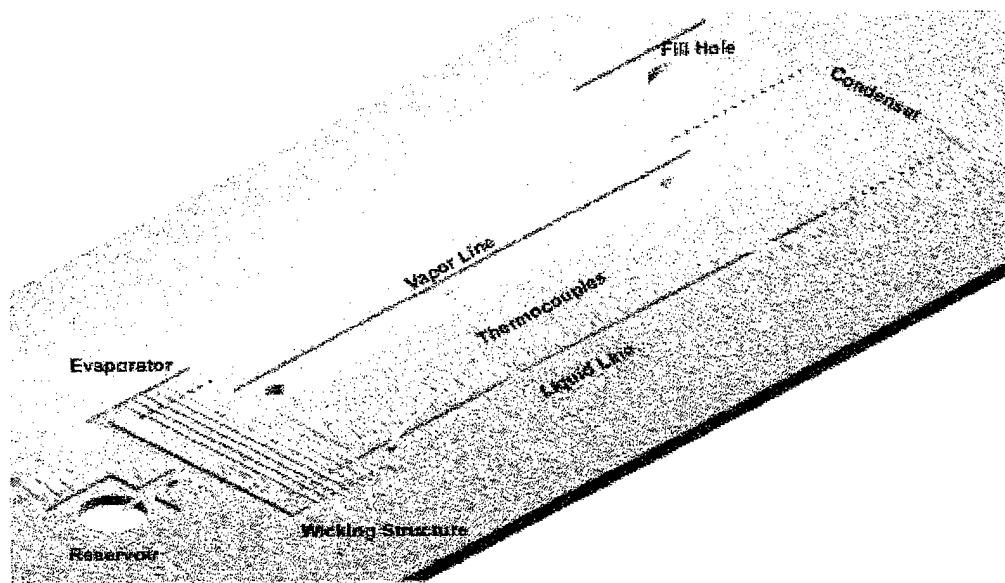
Figure 5.4 Second generation design of the micro-CPL

Evaporator Length	2000 μm
Evaporator Width	1000 μm
Condenser Area	2.5e+06 sq. μm
Groove Height	55 μm
Groove Width	90 μm
Average Groove Radius	50 μm
Number of Grooves	8
Vapor Line Dimensions	150 x 450 μm
Liquid Line Dimensions	150 x 150 μm
Vapor/Liquid Line Length	35 mm

Table 5.2 Geometric parameters for the second generation micro-CPL

V.2 Quantitative Experiments

The next set of experiments were quantitative in nature, were performed on the second generation micro-CPL. The micro-CPL was filled with water, and the reservoir pressurized to 15 psi above ambient. The device was operated in both the vertical (reflux) and horizontal orientation by applying a laser output 8.5 W (+/- 0.2 W) to the evaporator region, with a spot size diameter of 3.5 mm. Any laser output larger than 8.5 W (+/- 0.2 W) resulted in wick dry-out and device failure. A picture of the evaporator region when the micro-CPL was operating at steady-state in the vertical mode is shown in figure 5.5 Data collected from the thermocouples placed on the backside of the evaporator, liquid line, and condenser while in the vertical mode are shown in figure 5.6. Similarly, figures 5.7 and 5.8 show pictures of the evaporator region and temperature data for the horizontal mode.
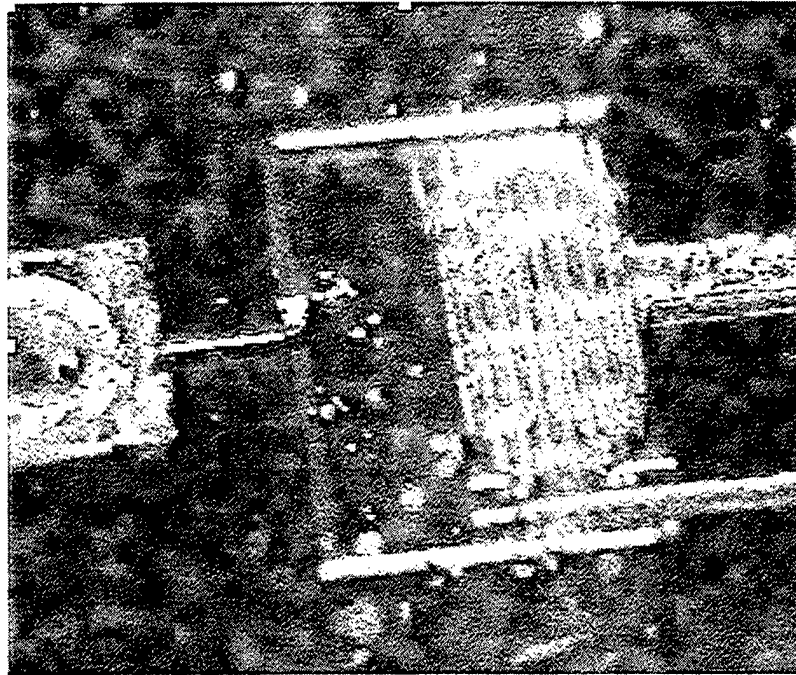
Figure 5.5 Evaporator region of the re-designed micro-CPL in vertical position
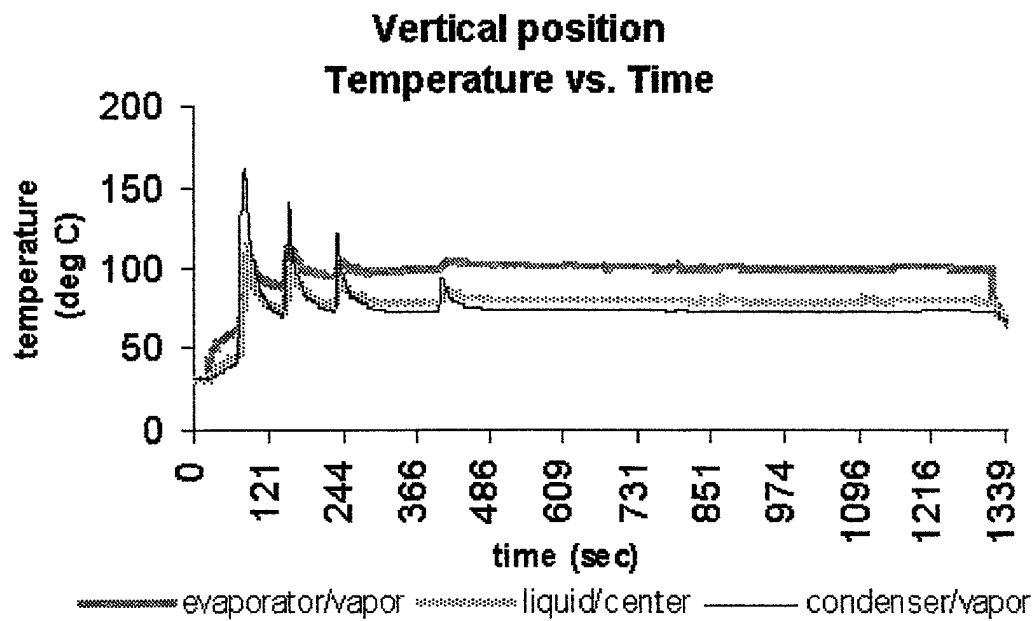
Figure 5.6 Temperature profile for the second generation micro-CPL operated in the vertical position with 3.5 mm diameter laser beam size
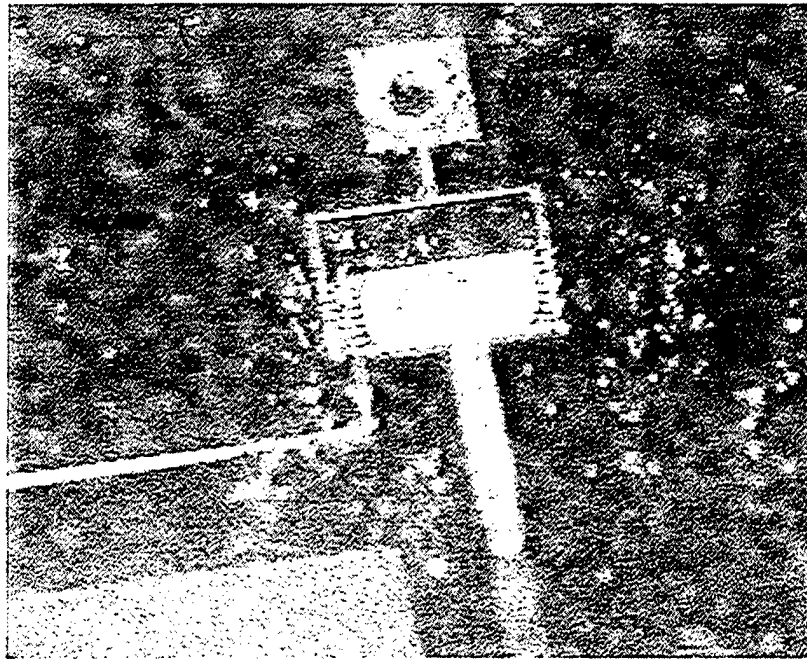
Figure 5.7 Evaporator region of the re-designed micro-CPL in horizontal position
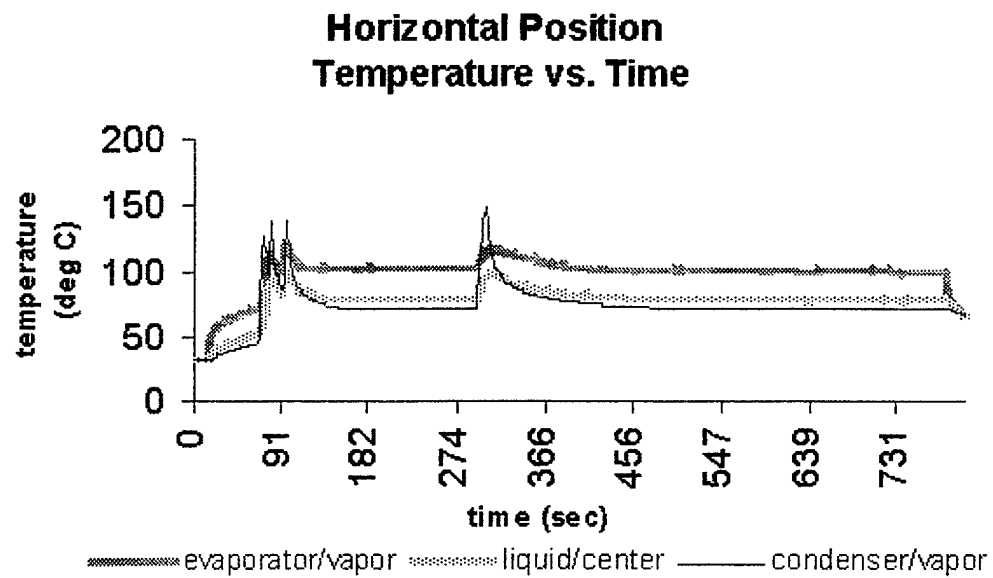
Figure 5.8 Temperature profile for the second generation micro-CPL operated in the horizontal position with 3.5 mm diameter laser beam size

There was no difference observed between the vertical and horizontal positioning of the micro-CPL. Once again, there were only two modes of operation in the evaporator, sensible heating and nucleate boiling. Figures 5.6 and 5.8 show the temperature initially increasing which is due to sensible heating of the fluid prior to the onset of nucleate boiling. The temperature spikes that appear during start-up are a direct result of the clearing of the vapor line with the micro-torch. As expected, body forces play little or no role in the micro-CPL, and regardless of orientation, the backside temperature of the evaporator was recorded at 100 C while the backside of the condenser was a lower 75 C.

The 25 degree temperature drop across the micro-CPL can be attributed to the large surface to volume ratios present, which as discussed earlier, result in non-isothermal vapor and liquid lines. Figure 5.7 clearly shows the early condensation that results from a non-isothermal vapor line. In fact, by examining figure 5.7, it is estimated that condensation is occurring only 2.0 mm away from the evaporator/vapor line port. The water was then observed to condense along the wall of the vapor line, reverse direction and return along the wall back into the evaporator. This can be considered to effectively reduce the size of the entire heat loop from 35 mm vapor/liquid lines to only 2.0 mm vapor/liquid lines. Due to the high thermal conductivity of silicon, and these large surface to volume ratios, it is an inescapable conclusion that something must be done to the micro-CPL in order to maintain isothermal vapor/liquid lines.

It is difficult to quantify exactly how much of the 8.5 W (+/- 0.2 W) entered the evaporator region due to the large spot size diameter. Recall, that the second generation micro-CPL has an evaporator size of 1000 µm x 2000 µm, which is smaller than the 3.5

59

mm diameter laser spot size being employed. The final set of experiments conducted

would need to have a significantly smaller beam diameter.

In the third set of experiments conducted, the laser spot diameter was reduced to

fit completely within the backside of the second generation micro-CPL's evaporator

region. After filling the micro-CPL with water, the reservoir was pressurized to 15 psi

above ambient. Similar to the previous experiments, there was no active cooling

mechanism used on the condenser other than natural convection, and the entire device

was exposed to the ambient with no insulation A laser output of 7.5 W (+/- 0.2 W) was

supplied to the evaporator region with a spot size diameter of 1.0 mm. Any laser output

larger than 7.5 W (+/- 0.2 W) resulted in wick dry-out and device failure. Data collected

from the thermocouples placed on the backside of the evaporator, vapor line, and

condenser are shown in figure 5.9.
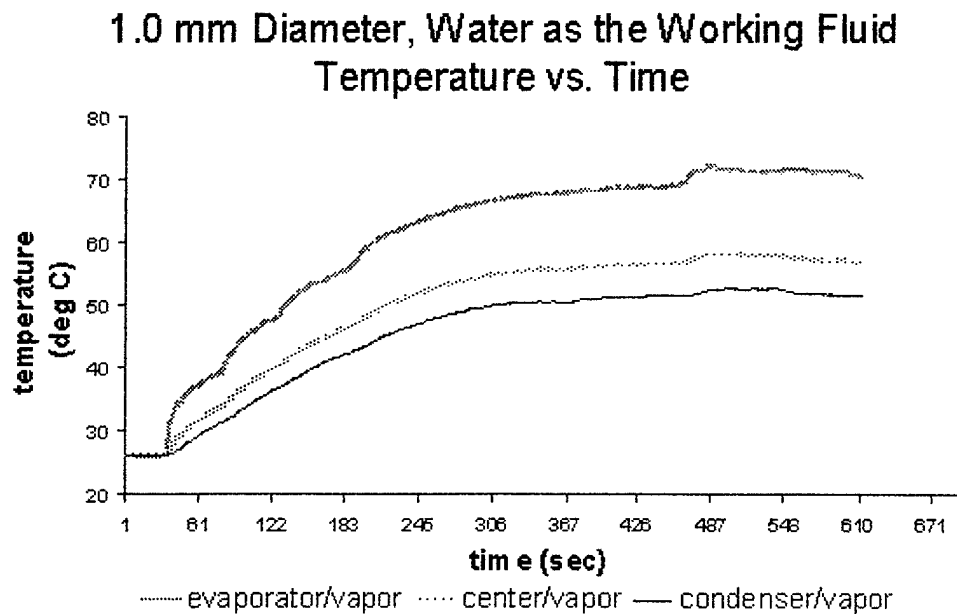
Figure 5.9 Temperature Profile for the "Filled" Case.

Although a smaller spot size diameter was used during these final experiments, the micro-CPL was observed to operate similar to the previous experiments with the 3.5 mm spot size diameter. Only two modes of operation where detected in the evaporator, sensible heating and nucleate boiling. Figure 5.9 reveals the time constant for the sensible heating mode of the evaporator, defined as the length of time for the evaporator temperature to reach 63.2% of the total temperature increase, to be approximately 350 s. The non-adiabatic nature of the vapor line resulted in early condensation within the vapor line. In fact, almost identical to the previous experiments, the final vapor/liquid condensation interface was 2.0 mm away from the evaporator/vapor line port. The water was then observed to condense along the wall of the vapor line, reverse direction and return along the wall back into the evaporator. Using the video footage, it is estimated that one quarter of the vapor line is being used to return liquid to the evaporator. Therefore the vapor line has an effective width of only 340 µm (designed to be 450 µm wide), while the liquid line is now only 110 µm wide (designed to be 150 µm wide). The thermocouples recorded the average temperature on the silicon wafer away from the evaporator region at 328 K (55 C), which is substantially higher than the 293 K (20 C) room temperature.

The temperature data presented in figure 5.9 illustrates the high delta T's which these uninsulated micro-CPLs are observed to support. The temperature in the evaporator region during steady state operation was 344 K (71 C), and the temperatures in the middle of the vapor line and condenser region were 331 K (58 C) and 325 K (52 C) respectively. This 19 degree temperature drop across the micro-CPL can once again be

directly attribute to the high surface to volume ratios within the device, and the resulting non-isothermal vapor line. It was these numbers, including the effective widths of the liquid and vapor lines, which were used in the sensitivity analysis previously presented in Chapter II.

In order to quantify the cooling effect on the evaporator region which the micro-CPL produces, the same laser spot size and output were used on two other configurations. First, the 7.5 W (+/- 0.2 W) output was focused on a micro-CPL which was unfilled, essentially using air as its working fluid. The temperature data presented in figure 5.10 shows the time constant of sensible heating was approximately 350 s, with an evaporator temperature of 351 K (78 C). Second, this same laser output was focused on a set of blank wafers (as explained in the previous chapter) on the spot where the evaporator region would be if a micro-CPL had been fabricated between the two wafers (30 mm from the center of the wafer). Figure 5.11 shows that the temperature recording on the backside of this laser spot, referred to as "Center", was an even higher 377 K (104 C). The length of sensible heating time constant was approximately 150 s. Comparing these results with micro-CPL utilizing water as the working fluid leads to the conclusion that the filled micro-CPL has a cooling effect of at least 7 degrees.

1.0 mm Diameter, Air as Working Fluid
Temperature vs. Time

—— evaporator/vapor ······· center/vapor —— condenser/vapor
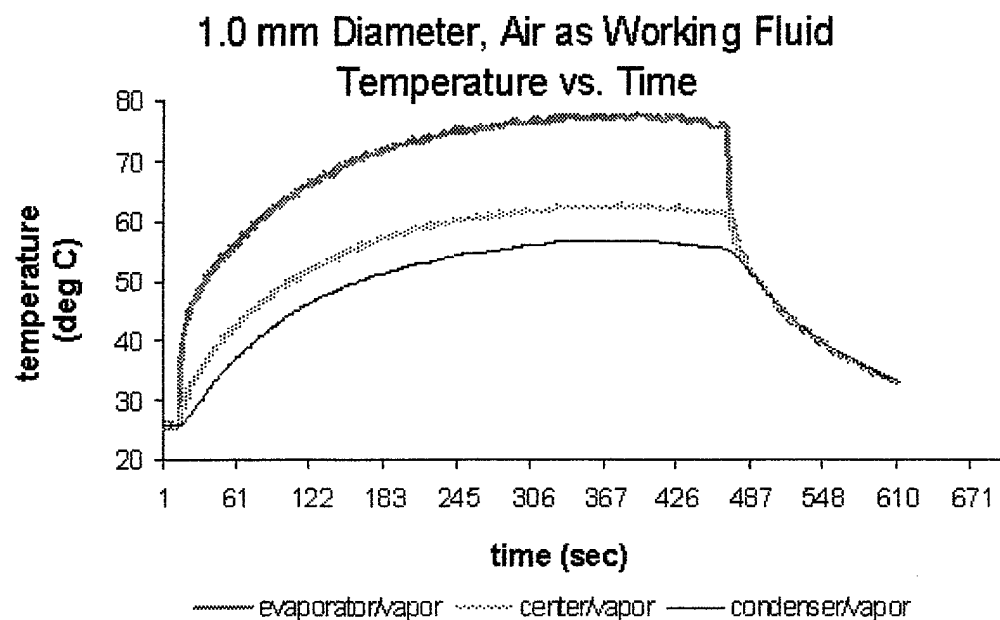
Figure 5.10 Temperature Profile for the "Unfilled" Case

1.0 mm Diameter, Blank Wafers
Temperature vs. Time

······ outboard,15mm —— center,0mm —— inboard,11mm
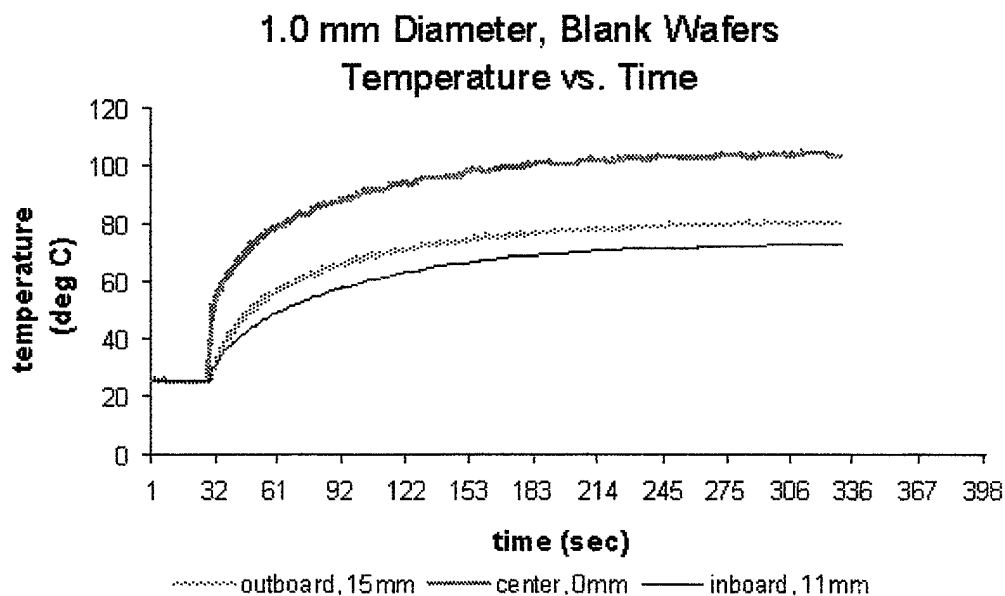
Figure 5.11 Temperature Profile for the "Blank" Case

In order to quantify how much heat the micro-CPL is transporting, a more thorough examination of the steady-state losses in the system is required. In the second set of experiments, a maximum laser output of 8.5 W (+/- 0.2 W) delivered over a spot size diameter of 3.5 mm was recorded prior to wick dry-out for the filled micro-CPL. However, in the third set of experiments a smaller laser diameter of 1.0 mm resulted in wick dry-out if the laser power exceed 7.5 W (+/- 0.2 W). In other words, while the heat flux entering the backside of the wicking structure on the glass wafer of the micro-CPL had increased dramatically from 8.8×10^5 W/m^2 to 9.5×10^6 W/ m^2, little change in micro-CPL performance was observed. This indicates that a substantial amount of the heat impacting the glass wafer is, in fact, not entering the micro-CPL evaporator, but instead is being "lost" to the ambient through convection off the front and backside of the wafers. An order of magnitude calculation based on the thermal mass of the wafers, and the corresponding heat convecting off the wafers due to natural convection reveals some deal of insight into the losses of the system.

The thermal mass of an object is defined as

$$m_{thermal} = \rho V c_p \qquad (5.1)$$

if a constant specific heat, density and temperature within the object are assumed. This is often thought of as an object resistance to heating or cooling. The wafers have a thickness of 500 μm and a radius of 0.1 m, and therefore they have identical volumes of 3.93×10^{-6} m^3. Therefore, the thermal mass of the two wafer configurations tested in all the experiments, neglecting the micro-CPL, can be written as

$$m_{thermal-glass} = (2225\frac{kg}{m^3})(3.93x10^{-6}m^3)(835\frac{J}{kg-K}) = 7.3\frac{J}{K}$$

$$m_{thermal-silicon} = (2330\frac{kg}{m^3})(3.93x10^{-6}m^3)(702\frac{J}{kg-K}) = 6.43\frac{J}{K}$$

$$m_{thermal} = m_{thermal-glass} + m_{thermal-silicon} = 7.3 + 6.43 = 13.73\frac{J}{K} \qquad (5.2)$$

Similarly, the thermal mass of the water filled micro-CPL, comprised of the working fluid within the device is several orders of magnitudes lower at

$$m_{thermal-CPL} = (957.9\frac{kg}{m^3})(3.87x10^{-9}m^3)(4181\frac{J}{kg-K}) = 1.5x10^{-2}\frac{J}{K} \qquad (5.3)$$

The temperature data for the micro-CPL filled with water, figure 5.9, reveals that the lowest temperature recorded on the wafer during steady state was 328 K (55 C). In fact, this was the lowest temperature recorded on any wafer configuration running at steady state. While the wafers support high thermal gradients, and the temperature is much higher in some places, this can be thought of as the base temperature in the wafers. In other words, during the steady-state runs, the wafers are heated to at least 328 K (55 C). If the ambient temperature is assumed to be 293 K (20 C), then enough heat must be constantly entering the wafer configuration to balance the heat being lost by convection (assuming that losses from beam reflection and radiation are negligible). Following the analysis presented in Chapter II for free convection on a vertical surface, the Grashof number is

$$Gr = \frac{g\beta(T_s - T_{inf})L^3}{v^2} = \frac{(9.8)\left(\dfrac{1}{310.5}\right)(328 - 293)(0.1)^3}{(16x10^{-6})^2} = 4.3x10^6 \qquad (5.4)$$

The Prandtl number, $Pr = v/\alpha = 0.7$ (Incorpera and DeWitt, 1981, p. 312). Therefore $GrPr = (4.3x10^6)(0.7) = 3.0x10^6$, and it was determined that $Nu = 22.4$ (Incorpera and DeWitt, 1981, p. 493). Using $L = 0.1$ m, and $k_{air} = 30 \times 10^{-3}$ W/m-K, $h = 6.7$ W/m^2-K.

As stated earlier, the wafers support a high thermal gradient during steady state. The calculation of the Grashof number, and the corresponding constant of natural convection, used the diameter of the wafers as the appropriate length scale. However, as demonstrated in the numerical analysis in Chapter II, smaller length scales can be selected based on spot size diameter, leading to larger values for h. Therefore, a sensitivity analysis of total heat convecting off the wafers based on h is presented. The total surface area exposed to the ambient is twice the surface area of one side of a wafer (two surfaces are exposed to quiescent air), the total losses to convection are

$$Q_{convection} = hA(T_s - T_{ambient}) = (h)(1.6x10^{-2})(328 - 293) \qquad (5.5)$$

A graph of total heat losses from convection based on different coefficients of convection is displayed in figure 5.12.

66

Coefficient of Natural Convection vs. Total Convective Heat Losses
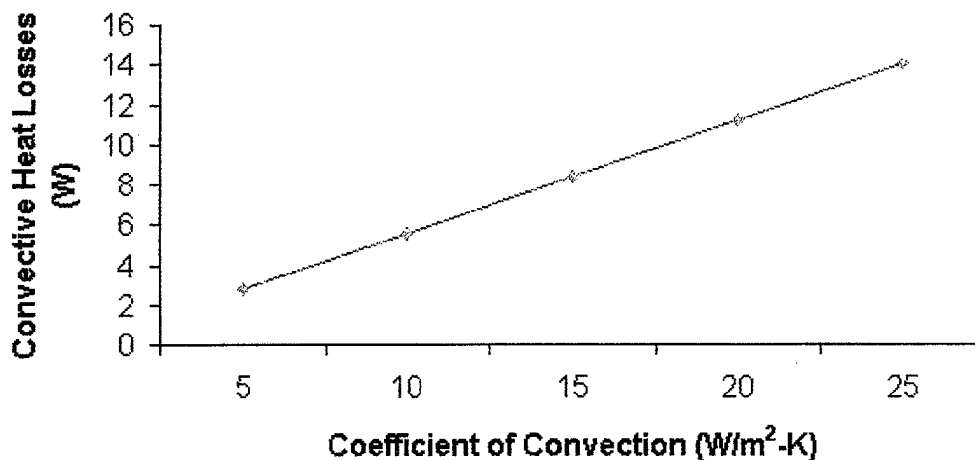
Figure 5.12 Sensitivity of convective losses to the coefficient of natural convection

In order for the thermal mass of wafers to support the base temperature present during micro-CPL operation, the laser must deliver a power of 3.7 W if the coefficient of natural convection is assumed to be $h = 6.7$ W/m^2-K. If the coefficient of convection is actually higher, so is are the losses due to convection. Therefore at least half, and perhaps most all, of the 7.5 W (+/- 0.2 W) being delivered by a laser spot size diameter of 1.0 mm is actually being convected off the wafers, and not entering the micro-CPL. Accordingly, there is no accurate way at present to determine the total heat the micro-CPL is transporting.

The large amount of heat the wafers are convecting to the ambient is further confirmed by examining transient responses of the wafer configurations, specifically the

67

sensible heating time constant of the blank wafers versus the micro-CPL runs. Recall that the sensible heating time for the blank wafers was on the order of 150 s, while it was on the order of 350 s for the micro-CPL configurations. Table 5.3 is a summary of the three experiments with their respective time constants.

Micro-CPL Design	Heat Source	Spot Size Diameter	Power Output	Orientation	Working Fluid	Sensible Heating Const.	Res. Pressure
None – Blank Wafers	CO_2 Laser	1.0 mm	7.5 W (+/- 0.2 W)	N/A	N/A	150 s	N/A
Second Generation	CO_2 Laser	1.0 mm	7.5 W (+/- 0.2 W)	Horizontal	Air	350 s	Amb
Second Generation	CO_2 Laser	1.0 mm	7.5 W (+/- 0.2 W)	Horizontal	Water	350 s	15 psi

Table 5.3 Sensible heating time constants

The amount of time required for sensible heating is clearly a function of thermal mass. While the heating of the blank wafers is not exactly a lumped capacitance situation, utilizing the predicted sensible heating time constant for a lumped capacitance method confirms the effect of the thermal mass of the wafers. The time constant for sensible heating of the wafer configuration, assuming lumped capacitance, is

68

$$t_{sensible} = \frac{m_{thermal}}{hA_s}$$

Thus, $t_{sensible}$ for the blank wafers is calculated at 130 s, using $h = 6.7$ W/m^2-K and a surface area equal to twice the surface area of one side of a wafer. This validates the idea that the thermal mass of the wafers is driving the sensible heating, recorded at approximately 150 s for the blank wafer configuration.

The thermal mass of the filled micro-CPL is three orders of magnitude lower than that of the blank wafers. If the micro-CPL was driving the experiments, one would expect this sensible heating time to reflect the huge differences in thermal mass. While the sensible heating time was doubled to approximately 350s, which indicates that the micro-CPL is having some effect, it does not change the amounts one would predict based on the change in thermal mass. This, in turn, confirms that the thermal mass of the wafers are in fact absorbing much of the laser power impacting the glass.

Finally, a second generation micro-CPL was coated with the FDTS SAM by coating the entire device after the anodic bonding was complete. As explained in Chapter II, this was done with the goal of reducing the surface tension force trying to "pull" the vapor/liquid condensation interface in the vapor line towards the evaporator region. Such a coating in the vapor line would aid during start-up by allowing this interface to move more freely towards the condenser region. The coated micro-CPL was flooded with water, and the reservoir was pressurized to 15 psi above ambient. The spot size diameter

of 1.0 mm was focused on the evaporator region, and the laser power slowly ramped up. The device completely failed, well before 7.5 W (+/- 0.2 W) was reached, due to the non-wetting, wicking structure in the glass. Water cannot be "drawn" into the axial groves in the glass, thereby resulting in wick dry-out. However, this "fully-coated" run did reveal the success of the FTDS SAM in the vapor line. The vapor/liquid condensation interface was observed to have a contact angle of almost 120°, resulting in a straight line interface. Figure 5.13 illustrates the wick dry-out and vapor/liquid interface observed in the "Fully-Coated" run, and figure 5.14 is the temperature data collected during this final run.
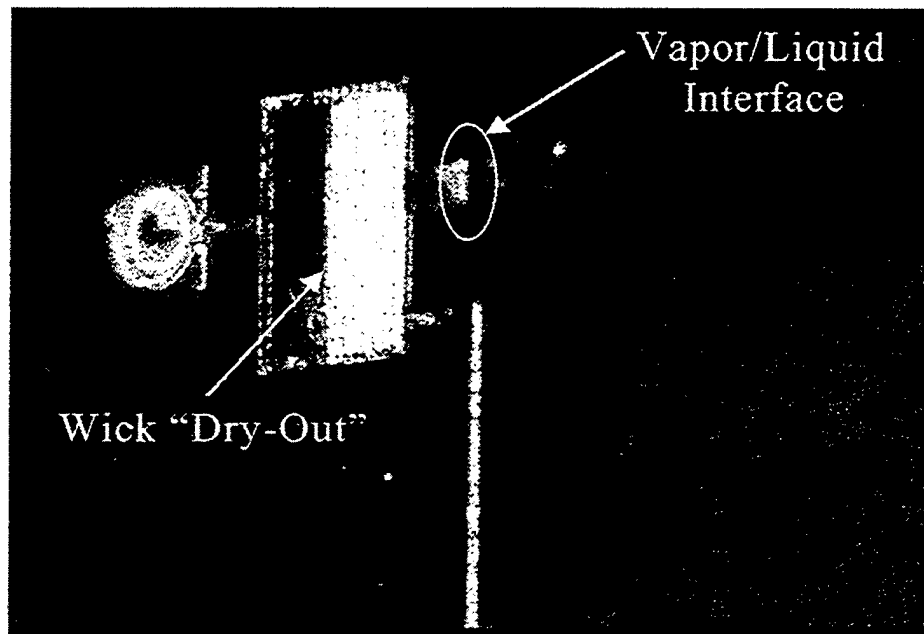
Figure 5.13 Evaporator Region during the "Fully-Coated" case

1.0 mm Diameter, FDTS SAM with Water
Temperature vs. Time

evaporator/vapor ⋯⋯ center/vapor —— condenser/vapor
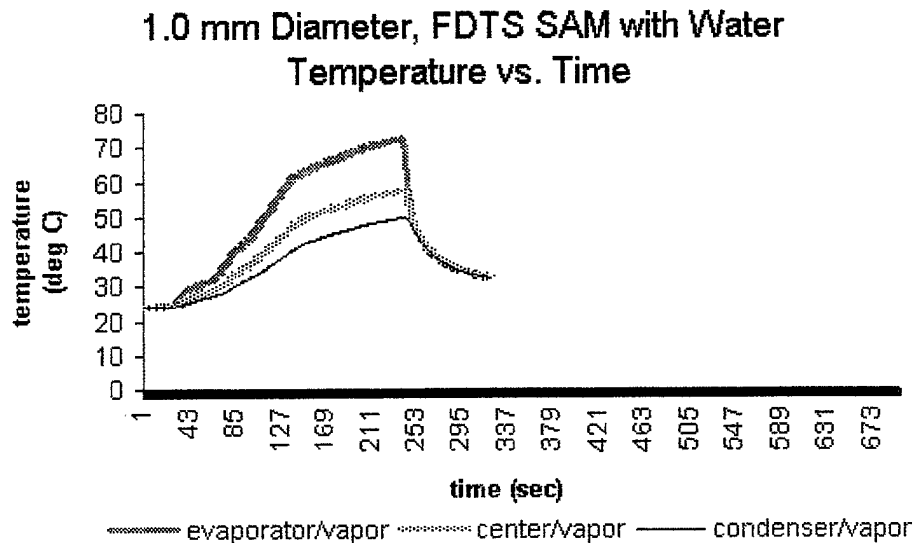
Figure 5.14 Temperature Profile for the "Fully Coated" Case.

V.3 Error Analysis

In order to evaluate the accuracy of the data presented at the end of the previous

chapter, the sources of error in the experiments must be examined. Both the laser output

and temperature data have distinct sources of uncertainty, which effect the accuracy of

the numbers presented.

As reported in section IV.1, the laser output is measured with a Newport power

meter. Although the laser power was fixed for all steady-state runs reported in chapter IV,

the calorimeter shows small fluctuations in its power vs. time data. The uncertainty in the

calorimeter can be quantified as twice the amplitude of these fluctuations. This peak-to-

71

peak magnitude was recorded as 0.2 W, therefore giving the uncertainty of laser power at +/- 0.2 W.

The thermocouples used were standard type E nickel/chromium-constantan Omega thermocouples. They were used off the shelf with a power meter, and were not calibrated separately. They are assumed to have an accuracy of +/- 1.0^{o}, however this could be improved if they were calibrated using a standard RTD precision thermometer and steady circulating bath set-up.

Chapter VI. Conclusion and Future Direction

Utilizing current MEMS technologies, a three-port micro-capillary pumped loop was designed, fabricated and tested to provide integral cooling to electronics or MEMS type devices. The two wafer design consists of one silicon and one borofloat glass wafer. A one-dimensional analytical study was used to determine the geometry of the device, including the evaporator dimensions (1000 μm x 2000 μm) and the length of the liquid and vapor lines.

Using a laser delivering 7.5 W (+/- 0.2 W) with a spot-size diameter of 1.0 mm, several devices were run near steady state. The micro-CPL was exposed to quiescent air, and the condenser region was not actively operated. When the laser was focused on a standard glass wafer anodically bonded to a single crystal silicon wafer, a backside silicon temperature of 377 K resulted. When the micro-CPL was present and fabricated between the two wafers but filled only with air, the backside temperature decreased to 351 K. Finally when a micro-CPL was filled with water the backside temperature dropped to 344 K. This 7 K backside cooling effect could be very useful in optimizing certain electronic packages.

The micro-CPL evaporator was observed to have only two modes of operation, sensible heating or nucleate boiling. The one-dimensional analytical study based on evaporation with no bubbles therefore fails to fully predict the larger pressure drop with bubbles present across the glass wicking structure. In order to better predict the total heat

transport rate of the micro-CPL, the evaporator wicking structure needs to be further studied. A pressure drop relationship based on nucleate boiling needs to be determined, in order to more accurately calculate the capillary pumping limit of the device.

It might be desirable to selectively coat the micro-CPL in order to enhance its performance, and aid during start-up. While the FDTS SAM hydrophobic coating of the entire device clearly reduced surface tension forces within the vapor line, it also made the wicking structure non-wetting, resulting in device failure. The micro-CPL should be selectively coated, allowing for a hydrophobic vapor line and evaporator/condenser plenums, while the rest of the device maintains its hydrophilic nature.

The small length scales in the micro-CPL, which make it such an attractive choice for chip-level thermal control, also result in the high surface area to volume ratios which inhibit the device's performance. A MEMS based micro-CPL allows for integration directly into whichever electronic package requires cooling. Since the micro-CPL is fabricated from silicon, there is no thermal mismatch between the micro-CPL and the electronic package. However, it is the large surface area to volume ratio in the vapor line which make it difficult to move the targeted heat long distances. The non-isothermal vapor line results in the micro-CPL supporting a rather large temperature difference between the evaporator and condenser regions. For this to be reduced, either heaters could be added to the vapor line to replace the heat being convected off the backside of the silicon, or the vapor line could be insulated. These changes would diminish the premature condensation in the vapor line, which was observed in the micro-CPL.

The experimental set-up needs to be further refined to remove the heat losses from the system in order to better quantify the heat transfer capacity of the micro-CPL. Presently the micro-CPL was tested while still part of an entire wafer, essentially connecting the device to a huge heat sink. In future tests, the wafer should be diced, allowing for each micro-CPL to be tested individually, and tested in a vacuum chamber to eliminate the convective heat losses necessary to sustain the thermal mass of the device in quiescent air. Only then can the analytical capillary pumping limit of the micro-CPL be verified. Finally, a thermal imaging system should be used. This would give temperature data for the liquid in the micro-CPL.

The micro-CPL shows exceptional promise in handling high thermal loads which electronic packages produce. Once the capillary pumping limit can be verified, other limits such as the boiling limit, can be further investigated, and the micro-CPL can be better understood.

Bibliography

Blevins, R.D., 1984, <u>Applied Fluid Dynamics Handbook</u>,Van Nostrand Reinhold Company, New York

Carey, V.P., 1992, <u>Liquid-Vapor Phase-Change Phenomena</u>, Hemisphere Publishing Corporation, Washington D.C., p. 82..

CFD-ACE+ Getting Started Guide, Version 5, October 1998. CFD Research Corporation, Huntsville, AL.

Dickey, J.T. , and Peterson G.P. , 1994,"Experimental and Analytical Investigation of a Capillary Pumped Loop," *Journal of Thermophysics and Heat Transfer*, Vol 8, No. 3, pp. 602-607.

Faghri, A., 1995, <u>Heat Pipe Science and Technology</u>, Taylor & Francis, Washinton D.C.

Hoelke, A., Henderson, H.T., Gerner F.M., Kazmierczak, M., 1999 "Analysis of the Heat Transfer Capacity of a Micromachined Loop Heat Pipe," *Proceedings of the ASME Heat Transfer Division,* HTD-Vol. 364-3 pp. 53-60.

Laub, J.H., and McGinness, H.D., "Recirculation of a Two-Phase Fluid by Thermal and Capillary Pumping," California Institute of Technology, Jet Propulsion Lab., TR 32-196, Pasadena, CA, Dec 1961.

Kirshberg, J., Yerkes, K., and Liepmann, D., 1999 "Micro-Cooler for Chip-Level Temperature Control," SAE *Aerospace Power Systems Conference*, P-341.

Ku, J. "Operating Characteristics of Loop Heat Pipes,", SAE paper No. 1999-01-2007, 1999.

Peterson, G.P., Duncan, A.B., and Weichold, M.H., 1993, "Experimental Investigation of Micro Heat Pipes Fabricated in Silicon Wafers," *Journal of Heat Transfer*, Vol 115, pp. 751-756.

Shah, R.K., and Bhatti, M.S., 1987, "Laminar Convective Heat Transfer in Ducts," in *Handbook of Single-Phase Convective Heat Transer,* Wiley, New York.
Madou, M., 1997, <u>Fundamentals of Microfabrication,</u> CRC Press, pp.384-386.

Srinivasan, U., Houston, M., Howe, R., and Maboudian, R., 1997 "Self-Assembled Fluorocarbon Films for Enhanced Stiction Reduction," *Transducers Digest of Technical Papers,* Vol. 2, pp. 1399-1402, 4D2.01.

Stenger, F.J. "Experimental Feasibility Study of Water-Filled Capillary-Pumped Heat-Transfer Loops," NASA TM X-1310, August 1966.

Appendix A – Numerical Analysis for Design of the Micro-CPL

A.1 Java Code Used to Determine Length of Liquid/Vapor Line

```
/***********************************************************
*Attempt to do the itterative mass
*flow calculations for the micro cpl
*by Jeff Kirshberg


***********************************************************/

    import java.awt.event.*;
    import javax.swing.*;
    import java.awt.*;
    import java.io.*;
    import java.text.*;

//CCCCCCC definition of class of objects needed to make windows closeable
    class Terminator extends WindowAdapter
    {
    public void windowClosing(WindowEvent e) {System.exit(0);}
    // this overrides the windowClosing method for WindowAdapter
    }
//EEEEEEEEEEEEEEEEEEEEEEEEEEEEEEEEEEEEEEEEEEEEEEEEEEEE

//CCCCCCC definition of class cplharris with the method main
// (where everything starts)
    public class thesis
{
public static void main(String[] args) // main() where it all begins
{
    // Uncomment the lines below to reassign standard output to
    // a file named cplout.txt
    try
        {FileOutputStream fs1 = new FileOutputStream("cplout.txt");
        System.setOut(new PrintStream(fs1));}
        catch(IOException e)
        { System.out.print("Error: " + e);
         System.exit(1);
        }

    // BBBBBBBBBBBB Definition of constants
        double CP = 4217.; // Cp at Ts for water
        double HFG = 2257000.; //Hfg for water
        double WE = .001; //Width of the Evaporator
        double LE = .0005; //Length of the Evaporator
        double WC = .0005; //Width of the Condenser
        double LC = .001; //Length of the Condenser
        double HC = 10.; //Coefficient of Convection for the Condenser
        double TSAT = 373.; //Sat temp for Water
        double TWALLC = 370.; //Twall of the condenser
        double DEPTH = .00015; //Depth of both Liquid and Vapor Lines
        double WLIQ = .00015; //Width of Liquid Line
```

77

```
double WVAP = .00045; //Width of Vapor Line
double RHOV = .59559; //Density of Vapor at Tsat
double RHOL = 957.8544; //Density of Liquid at Tsat
double VISCL = 0.000279; //Viscosity of liquid at Tsat
double VISCV = 0.00001202; //Viscosity of vapor at Tsat
double HGROOVE = .000045; //Height of Groove
double WGROOVE = .000045; //Width of Groove
double SGROOVE = .00005; //Space between Grooves
double NG = 4.; //Number of Grooves
double SURFT = 0.0589; //Surface Tension at Tsat
double PV = 101330.; //Sat Pressure at Tsat
double R = 461.3929; //Gas Constant for Water
double TLIQ = 370.;  //Liquid Temp (fixes Delta T at 3 degrees)

double HDV, HDL, AC, AE, WASPECT, FGROOVE;
HDV = 4 * (DEPTH * WVAP) / ((2*DEPTH) + (2*WVAP));//Hydraulic Diameter of Vapor Line
HDL = 4 * (DEPTH * WLIQ) / ((2*DEPTH) + (2*WLIQ));//Hydraulic Diameter of Liquid Line
AC = LC*WC; //Area of Condenser
AE = LE*WE; //Area of Evaporator
WASPECT = WGROOVE/HGROOVE; //Aspect Ratio Wick
    FGROOVE = 24*(1-(1.3553*WASPECT)+(1.9467*WASPECT*WASPECT)-
    1.7012*WASPECT*WASPECT*WASPECT)+(0.9564*WASPECT*WASPECT*WASPECT*W
    ASPECT)-(0.2537*WASPECT*WASPECT*WASPECT*WASPECT*WASPECT));
            //Friction factor for wick

double LLIQ, LVAP, LSTEP, VVAPMAX, MDOTMAX, QTOTMAX;
LLIQ = .005; // initial length of liquid line
LVAP = .005; // inital length of vapor line
LSTEP = .005;
    // Keeping in mind REV < 3300 to stay laminar, we must look
    //  at a max velocity and determine Qtot that way as well
VVAPMAX = 3300 * VISCV / (HDV * RHOV);
MDOTMAX = VVAPMAX * (RHOV*DEPTH*WVAP);
QTOTMAX = MDOTMAX*HFG + (MDOTMAX*CP*(TSAT - TLIQ));

while (LLIQ < 1.00001) // Steeping loop for different line lengths
{
// The second while loop will be one which marches through different vapor
// and liquid line lengths to gather data about Qtot vs distance
    //Because we think that the Capillary Pumping limit
    //Will be the limiting factor
    //Using our geometry we can calculate the maximum velocities
    //Our device can support.
    //We will set up a Newton Rapson scheme which guesses solves
    //for maximum velocities, and then checks to make sure that this
    //value is below the maximum heat transfer that the quadratic equation
    //which governs heat transfer allows


double PCAP, PTEMP, VELV, VELL, REV, REL, FVAP, FLIQ;
 double MDOT, MDOT2, VELV2, VELL2, REV2, REL2, FCNM, FCNM2, STEP, DERIV,
 ERROR, ITER;
double FVAP2, FLIQ2, PVAP, PLIQ, PVAP2, PLIQ2, PWIC, PWIC2, RATIOV, RATIOL;
MDOT = .1; //Original Guess of MDOT
ERROR = 10.; // Initializing error funtion so the while loop starts
STEP = .0000000000001; //Step size for Newton Rapson
```

```
FCNM = 0.; //Initializing the variable
DERIV = 1.; //Initializing
ITER = 0.; //Counting number of times Newton Scheme Runs
REV = 0.; //Initializing
REL = 0.; //Initializing
PWIC = 0.;//Initializing
PLIQ = 0.; //Initializing
PVAP = 0.; //Initializing
PCAP = 0.; //Initializing
PTEMP = 0.; //Initializing
while ((ERROR * ERROR) > .000000000000001) // Error function for Newton Rapson
{
  MDOT -= FCNM/DERIV;
  MDOT2 = MDOT + STEP;
  PCAP = 2 * SURFT / WGROOVE; //Capillary Pressure Head
  PTEMP = (PV * HFG * (TSAT - TLIQ))/ (R * TSAT * TSAT); //Temp Pressure Head
  VELV = MDOT/(RHOV*DEPTH*WVAP); //Vapor Line Velocity
  VELL = MDOT/(RHOL*DEPTH*WLIQ); //Liquid Line Velocity
  VELV2 = MDOT2/(RHOV*DEPTH*WVAP);
  VELL2 = MDOT2/(RHOL*DEPTH*WLIQ);
  REV = VELV * HDV * RHOV / VISCV; // Reynolds number in vapor line
  REL = VELL * HDL * RHOL / VISCL; // Reynolds number in liquid line
  REV2 = VELV2 * HDV * RHOV / VISCV;
  REL2 = VELL2 * HDL * RHOL / VISCL;
  RATIOV = DEPTH/WVAP; //Aspect ratio in Vapor line
  RATIOL = DEPTH/WLIQ; //Aspect ration in Liquid Line
          FVAP = (((2 - RATIOV)*RATIOV*11/24) + .6666666666667)*64/REV; //Friction
          factor for vapor line
          FLIQ = (((2 - RATIOL)*RATIOL*11/24) + .6666666666667)*64/REL;//Friction facotr
          for liquid line
          FVAP2 = (((2 - RATIOV)*RATIOV*11/24) + .6666666666667)*64/REV2;//Friction
          factor for vapor line
          FLIQ2 = (((2 - RATIOL)*RATIOL*11/24) + .6666666666667)*64/REL2;//Friction
          facotr for liquid line
  PVAP = FVAP*RHOV*VELV*VELV*LVAP/(2*HDV); //Pressure Loss in Vapor Line
  PLIQ = FLIQ*RHOL*VELL*VELL*LLIQ/(2*HDL); //Pressure Loss in Liquid Line
  PVAP2 = FVAP2*RHOV*VELV2*VELV2*LVAP/(2*HDV);
  PLIQ2 = FLIQ2*RHOL*VELL2*VELL2*LLIQ/(2*HDL);
          PWIC = VISCL*FGROOVE*LE*(2*HGROOVE + WGROOVE)*(2*HGROOVE +
          WGROOVE)*((HFG*MDOT)+(MDOT*CP*(TSAT -
          TLIQ)))/(8*RHOL*HFG*NG*(HGROOVE*WGROOVE)*(HGROOVE*WGROOVE)*
          (HGROOVE*WGROOVE));//pressure drop through the wick
          PWIC2 = VISCL*FGROOVE*LE*(2*HGROOVE + WGROOVE)*(2*HGROOVE +
          WGROOVE)*((HFG*MDOT2)+(MDOT2*CP*(TSAT -
          TLIQ)))/(8*RHOL*HFG*NG*(HGROOVE*WGROOVE)*(HGROOVE*WGROOVE)*
          (HGROOVE*WGROOVE));
  FCNM = PCAP + PTEMP - (PLIQ + PVAP + PWIC);
  FCNM2 = PCAP + PTEMP - (PLIQ2 + PVAP2 + PWIC2);
  DERIV = (FCNM2 - FCNM) / STEP;
  ERROR = FCNM;
  ITER += 1.;
}

//Now Calculate Mdod from the quadradic governing equation
  double QTOT, A, B, C, MDOTROOT;
  QTOT = MDOT*HFG + (MDOT*CP*(TSAT - TLIQ));
```

79

```
A = CP*HFG/(AC*HC);
B = (HFG + (CP*TSAT) - ((CP*QTOT)/(AC*HC)) - (CP*TWALLC));
C = -1 * QTOT;
MDOTROOT = ((-1 * B) + Math.sqrt(B*B - (4*A*C)))/(2*A);
System.out.println(" LVAP=  "+ LVAP);
System.out.println(" LLIQ =  "+ LLIQ);
System.out.println(" ITER =  "+ ITER);
System.out.println(" MDOT=  "+ MDOT);
System.out.println(" MDOTROOT =  "+ MDOTROOT);
System.out.println(" REV =  "+ REV);
System.out.println(" REL =  "+ REL);
System.out.println(" QTOT=  "+ QTOT);
System.out.println(" PCAP =  "+ PCAP);
System.out.println(" PTEMP =  "+ PTEMP);
System.out.println(" PVAP =  "+ PVAP);
System.out.println(" PLIQ =  "+ PLIQ);
System.out.println(" PWIC=  "+ PWIC);
System.out.println(" ++++++++++++++++++++++++++++++++++++++++++++++++++++++ " );
System.out.println(" MDOTMAX = "+ MDOTMAX);
System.out.println(" QTOTMAX =  "+ QTOTMAX);


System.out.println(" ********************************************** " );

LLIQ += LSTEP;
LVAP += LSTEP;

}



} // end main() method


//EEEEEEEEEEEEEEEEEEEEEEEEEEEEEEEEEEEEEEEEEEEEEEEEEEEEEEEEEEEEEEEEEEEEEEEEEEEE
EEEEE
}
```

A.2 Output of Code for Micro-CPL Designed in Chapter II.


```
VAP= 0.0050
LLIQ = 0.0050
ITER = 4.0
MDOT= 1.1911371789626121E-5
MDOTROOT = 1.1978131101099413E-5
REV = 3303.209037611237
REL = 284.62059234471013
QTOT= 27.034656893696717
PCAP = 2617.777777777778
PTEMP = 10688.143735056057
PVAP = 10369.775391589868
```

PLIQ = 1233.5988450133411
PWIC= 1702.5472762306076
++
MDOTMAX = 1.1899799999999997E-5
QTOTMAX = 27.008392969799992
****
LVAP= 0.01
LLIQ = 0.01
ITER = 4.0
MDOT= 6.362756287340254E-6
MDOTROOT = 6.3984143434192284E-6
REV = 1764.4914829007917
REL = 152.03718727216855
QTOT= 14.441236170318094
PCAP = 2617.777777777778
PTEMP = 10688.143735056057
PVAP = 11078.548253964907
PLIQ = 1317.9151731289685
PWIC= 909.4580857399591
++
MDOTMAX = 1.1899799999999997E-5
QTOTMAX = 27.008392969799992
****
LVAP= 0.015
LLIQ = 0.015
ITER = 4.0
MDOT= 4.340733728964326E-6
MDOTROOT = 4.365057887793949E-6
REV = 1203.7531139668126
REL = 103.72123605649526
QTOT= 9.851950648677612
PCAP = 2617.777777777778
PTEMP = 10688.143735056057
PVAP = 11336.838761911717
PLIQ = 1348.641670111681
PWIC= 620.4410808104338
++
MDOTMAX = 1.1899799999999997E-5
QTOTMAX = 27.008392969799992
****
LVAP= 0.02
LLIQ = 0.02
ITER = 4.0
MDOT= 3.2939486340475664E-6
MDOTROOT = 3.312405324139136E-6
REV = 913.4632928584489
REL = 78.70845003697889
QTOT= 7.476113811214693
PCAP = 2617.777777777778
PTEMP = 10688.143735056057
PVAP = 11470.553716157545
PLIQ = 1364.548534714789
PWIC= 470.81926196153347
++
MDOTMAX = 1.1899799999999997E-5
QTOTMAX = 27.008392969799992

```
************************************************
LVAP= 0.025
LLIQ = 0.025
ITER = 4.0
MDOT= 2.6539404138890814E-6
MDOTROOT = 2.668809712443459E-6
REV = 735.9790387934224
REL = 63.415541550515684
QTOT= 6.023518514323768
PCAP = 2617.777777777778
PTEMP = 10688.143735056057
PVAP = 11552.307526267157
PLIQ = 1374.2740496770948
PWIC= 379.3399368895876
++++++++++++++++++++++++++++++++++++++++++++++++++
MDOTMAX = 1.1899799999999997E-5
QTOTMAX = 27.008392969799992
************************************************
LVAP= 0.030000000000000002
LLIQ = 0.030000000000000002
ITER = 4.0
MDOT= 2.222175719041503E-6
MDOTROOT = 2.234624878534756E-6
REV = 616.2439598007497
REL = 53.09858348964165
QTOT= 5.043563342898266
PCAP = 2617.777777777778
PTEMP = 10688.143735056057
PVAP = 11607.460581748019
PLIQ = 1380.835112281723
PWIC= 317.62581880408726
++++++++++++++++++++++++++++++++++++++++++++++++++
MDOTMAX = 1.1899799999999997E-5
QTOTMAX = 27.008392969799992
************************************************
LVAP= 0.035
LLIQ = 0.035
ITER = 4.0
MDOT= 1.9112396485423826E-6
MDOTROOT = 1.9219459409844416E-6
REV = 530.0165414704334
REL = 45.668808806269595
QTOT= 4.337846979553867
PCAP = 2617.777777777778
PTEMP = 10688.143735056057
PVAP = 11647.179147327603
PLIQ = 1385.5600725411612
PWIC= 273.1822929650922
++++++++++++++++++++++++++++++++++++++++++++++++++
MDOTMAX = 1.1899799999999997E-5
QTOTMAX = 27.008392969799992
************************************************
LVAP= 0.04
LLIQ = 0.04
ITER = 4.0
MDOT= 1.6766375482506794E-6
```

MDOTROOT = 1.6860288429622672E-6
REV = 464.95772275393216
REL = 40.06302385306283
QTOT= 3.805382088024703
PCAP = 2617.777777777778
PTEMP = 10688.143735056057
PVAP = 11677.146911731948
PLIQ = 1389.1250677470175
PWIC= 239.64953335486123
+++
MDOTMAX = 1.1899799999999997E-5
QTOTMAX = 27.008392969799992
****
LVAP= 0.045
LLIQ = 0.045
ITER = 4.0
MDOT= 1.49333293575479E-6
MDOTROOT = 1.5016967668599136E-6
REV = 414.12449688152805
REL = 35.682985322695096
QTOT= 3.389344590968795
PCAP = 2617.777777777778
PTEMP = 10688.143735056057
PVAP = 11700.56200236704
PLIQ = 1391.9105503319881
PWIC= 213.44896013480735
+++
MDOTMAX = 1.1899799999999997E-5
QTOTMAX = 27.008392969799992
****
LVAP= 0.049999999999999996
LLIQ = 0.049999999999999996
ITER = 4.0
MDOT= 1.3461591037437956E-6
MDOTROOT = 1.3536979925112591E-6
REV = 373.3108995407087
REL = 32.16628682780874
QTOT= 3.0553113559712095
PCAP = 2617.777777777778
PTEMP = 10688.143735056057
PVAP = 11719.361794520262
PLIQ = 1394.1469923966365
PWIC= 192.41127259169344
+++
MDOTMAX = 1.1899799999999997E-5
QTOTMAX = 27.008392969799992
****
LVAP= 0.05499999999999999
LLIQ = 0.05499999999999999
ITER = 4.0
MDOT= 1.22539191296634E-6
MDOTROOT = 1.2322538746456005E-6
REV = 339.82027536504165
REL = 29.280571397045165
QTOT= 2.781211980655966
PCAP = 2617.777777777778

83

PTEMP = 10688.143735056057
PVAP = 11734.788436977733
PLIQ = 1395.9821612020676
PWIC= 175.150914653915
+++
MDOTMAX = 1.1899799999999997E-5
QTOTMAX = 27.008392969799992
****
LVAP= 0.05999999999999999
LLIQ = 0.05999999999999999
ITER = 4.0
MDOT= 1.124509449080431E-6
MDOTROOT = 1.130805942102895E-6
REV = 311.843995862571
REL = 26.869998783283897
QTOT= 2.5522439956148495
PCAP = 2617.777777777778
PTEMP = 10688.143735056057
PVAP = 11747.675030518594
PLIQ = 1397.5151632496386
PWIC= 160.7313190656072
+++
MDOTMAX = 1.1899799999999997E-5
QTOTMAX = 27.008392969799992
****
LVAP= 0.06499999999999999
LLIQ = 0.06499999999999999
ITER = 4.0
MDOT= 1.0389741436668748E-6
MDOTROOT = 1.0447911923575802E-6
REV = 288.123722592034
REL = 24.8261444125896
QTOT= 2.358108704147666
PCAP = 2617.777777777778
PTEMP = 10688.143735056057
PVAP = 11758.601198177374
PLIQ = 1398.814951074862
PWIC= 148.5053635816021
+++
MDOTMAX = 1.1899799999999997E-5
QTOTMAX = 27.008392969799992
****
LVAP= 0.06999999999999999
LLIQ = 0.06999999999999999
ITER = 4.0
MDOT= 9.65531429779406E-7
MDOTROOT = 9.709368158730342E-7
REV = 267.75691341636326
REL = 23.07124085494399
QTOT= 2.1914193751302586
PCAP = 2617.777777777778
PTEMP = 10688.143735056057
PVAP = 11767.98267406467
PLIQ = 1399.9309808230553
PWIC= 138.00785794610564
+++

MDOTMAX = 1.1899799999999997E-5
QTOTMAX = 27.008392969799992
****
LVAP= 0.075
LLIQ = 0.075
ITER = 4.0
MDOT= 9.017862176630179E-7
MDOTROOT = 9.068342978696635E-7
REV = 250.07937261869603
REL = 21.548057769725638
QTOT= 2.046739990705086
PCAP = 2617.777777777778
PTEMP = 10688.143735056057
PVAP = 11776.12540380253
PLIQ = 1400.899648091203
PWIC= 128.89646094009333
++
MDOTMAX = 1.1899799999999997E-5
QTOTMAX = 27.008392969799992
****
LVAP= 0.08
LLIQ = 0.08
ITER = 4.0
MDOT= 8.459367488334485E-7
MDOTROOT = 8.506717805957791E-7
REV = 234.5914444906957
REL = 20.213542385506535
QTOT= 1.9199811879265851
PCAP = 2617.777777777778
PTEMP = 10688.143735056057
PVAP = 11783.259541655163
PLIQ = 1401.7483322606122
PWIC= 120.91363891807212
++
MDOTMAX = 1.1899799999999997E-5
QTOTMAX = 27.008392969799992
****
LVAP= 0.085
LLIQ = 0.085
ITER = 4.0
MDOT= 7.96601580196614E-7
MDOTROOT = 8.010600776535384E-7
REV = 220.91003333239436
REL = 19.03468530935756
QTOT= 1.808007573094825
PCAP = 2617.777777777778
PTEMP = 10688.143735056057
PVAP = 11789.561551350374
PLIQ = 1402.4980256327165
PWIC= 113.86193585074163
++
MDOTMAX = 1.1899799999999997E-5
QTOTMAX = 27.008392969799992
****
LVAP= 0.09000000000000001
LLIQ = 0.09000000000000001

ITER = 4.0
MDOT= 7.5270377381I2451E-7
MDOTROOT = 7.569162146187763E-7
REV = 208.73648746845396
REL = 17.985753257138473
QTOT= 1.708374872934466
PCAP = 2617.777777777778
PTEMP = 10688.143735056057
PVAP = 11795.168999527477
PLIQ = 1403.1650932724217
PWIC= 107.58742003393206
+++
MDOTMAX = 1.1899799999999997E-5
QTOTMAX = 27.008392969799992
****
LVAP= 0.09500000000000001
LLIQ = 0.09500000000000001
ITER = 4.0
MDOT= 7.133913780429714E-7
MDOTROOT = 7.173834644738149E-7
REV = 197.8345474328817
REL = 17.04638896160027
QTOT= 1.6191494545666083
PCAP = 2617.777777777778
PTEMP = 10688.143735056057
PVAP = 11800.190713370159
PLIQ = 1403.762481370272
PWIC= 101.96831809340951
+++
MDOTMAX = 1.1899799999999997E-5
QTOTMAX = 27.008392969799992
****
LVAP= 0.10000000000000002
LLIQ = 0.10000000000000002
ITER = 4.0
MDOT= 6.779815906314482E-7
MDOTROOT = 6.817751976958386E-7
REV = 188.01486151731783
REL = 16.200276956545952
QTOT= 1.538781595158257
PCAP = 2617.777777777778
PTEMP = 10688.143735056057
PVAP = 11804.713913143041
PLIQ = 1404.3005657361218
PWIC= 96.90703395467588
+++
MDOTMAX = 1.1899799999999997E-5
QTOTMAX = 27.008392969799992
****
LVAP= 0.10500000000000002
LLIQ = 0.10500000000000002
ITER = 4.0
MDOT= 6.459207644725913E-7
MDOTROOT = 6.495346638624147E-7
REV = 179.1238947511346
REL = 15.434187920492027

QTOT= 1.4660147090059814
PCAP = 2617.777777777778
PTEMP = 10688.143735056057
PVAP = 11808.80932100061
PLIQ = 1404.7877595481555
PWIC= 92.32443228506767
++
MDOTMAX = 1.1899799999999997E-5
QTOTMAX = 27.008392969799992
****
LVAP= 0.11000000000000003
LLIQ = 0.11000000000000003
ITER = 4.0
MDOT= 6.167552486492352E-7
MDOTROOT = 6.202056692394729E-7
REV = 171.03584266479072
REL = 14.737281927102394
QTOT= 1.3998191668519855
PCAP = 2617.777777777778
PTEMP = 10688.143735056057
PVAP = 11812.534885715671
PLIQ = 1405.230956450304
PWIC= 88.15567066785732
++
MDOTMAX = 1.1899799999999997E-5
QTOTMAX = 27.008392969799992
****
LVAP= 0.11500000000000003
LLIQ = 0.11500000000000003
ITER = 4.0
MDOT= 5.901097879301528E-7
MDOTROOT = 5.934108552045899E-7
REV = 163.64664113426312
REL = 14.100592304185254
QTOT= 1.3393432702854593
PCAP = 2617.777777777778
PTEMP = 10688.143735056057
PVAP = 11815.938541898984
PLIQ = 1405.6358587917716
PWIC= 84.3471121430791
++
MDOTMAX = 1.1899799999999997E-5
QTOTMAX = 27.008392969799992
****
LVAP= 0.12000000000000004
LLIQ = 0.12000000000000004
ITER = 4.0
MDOT= 5.656712895802266E-7
MDOTROOT = 5.688353740664268E-7
REV = 156.869464664511
REL = 13.51663774385249
QTOT= 1.2838764080670508
PCAP = 2617.777777777778
PTEMP = 10688.143735056057
PVAP = 11819.060283605628
PLIQ = 1406.0072243053269

87

PWIC= 80.8540049228788
+++
MDOTMAX = 1.1899799999999997E-5
QTOTMAX = 27.008392969799992
****
LVAP= 0.125000000000000003
LLIQ = 0.125000000000000003
ITER = 4.0
MDOT= 5.431764634036117E-7
MDOTROOT = 5.462144598275139E-7
REV = 150.631298780813
REL = 12.979126963049264
QTOT= 1.2328210033404707
PCAP = 2617.777777777778
PTEMP = 10688.143735056057
PVAP = 11821.933743179692
PLIQ = 1406.3490539282357
PWIC= 77.63871572590892
+++
MDOTMAX = 1.1899799999999997E-5
QTOTMAX = 27.008392969799992
****
LVAP= 0.13000000000000003
LLIQ = 0.13000000000000003
ITER = 4.0
MDOT= 5.22402298078277E-7
MDOTROOT = 5.253238511364733E-7
REV = 144.8702989679082
REL = 12.482731136876392
QTOT= 1.1856708982356596
PCAP = 2617.777777777778
PTEMP = 10688.143735056057
PVAP = 11824.587407794774
PLIQ = 1406.6647365231424
PWIC= 74.66936851592456
+++
MDOTMAX = 1.1899799999999997E-5
QTOTMAX = 27.008392969799992
****
LVAP= 0.13500000000000004
LLIQ = 0.13500000000000004
ITER = 4.0
MDOT= 5.031586424216244E-7
MDOTROOT = 5.059723309699402E-7
REV = 139.53373333933013
REL = 12.0229066289516
QTOT= 1.1419945159308824
PCAP = 2617.777777777778
PTEMP = 10688.143735056057
PVAP = 11827.045567113404
PLIQ = 1406.9571616125784
PWIC= 71.91878410788115
+++
MDOTMAX = 1.1899799999999997E-5
QTOTMAX = 27.008392969799992
****

LVAP= 0.14000000000000004
LLIQ = 0.14000000000000004
ITER = 4.0
MDOT= 4.852823680976576E-7
MDOTROOT = 4.879958566203724E-7
REV = 134.5763638651297
REL = 11.595755510099346
QTOT= 1.1014216120352167
PCAP = 2617.777777777778
PTEMP = 10688.143735056057
PVAP = 11829.329058935036
PLIQ = 1407.228808081995
PWIC= 69.36364581676278
++
MDOTMAX = 1.1899799999999997E-5
QTOTMAX = 27.008392969799992
****
LVAP= 0.14500000000000005
LLIQ = 0.14500000000000005
ITER = 4.0
MDOT= 4.6863273396012063E-7
MDOTROOT = 4.712528980552751E-7
REV = 129.9591608319802
REL = 11.19791478996704
QTOT= 1.0636327532653218
PCAP = 2617.777777777778
PTEMP = 10688.143735056057
PVAP = 11831.455861349172
PLIQ = 1407.481814622886
PWIC= 66.98383686177847
++
MDOTMAX = 1.1899799999999997E-5
QTOTMAX = 27.008392969799992
****
LVAP= 0.15000000000000005
LLIQ = 0.15000000000000005
ITER = 4.0
MDOT= 4.5308767301448677E-7
MDOTROOT = 4.556207040667643E-7
REV = 125.6482731598688
REL = 10.82646769449192
QTOT= 1.028350890145003
PCAP = 2617.777777777778
PTEMP = 10688.143735056057
PVAP = 11833.44156703336
PLIQ = 1407.7180361557594
PWIC= 64.76190964472377
++
MDOTMAX = 1.1899799999999997E-5
QTOTMAX = 27.008392969799992
****
LVAP= 0.15500000000000005
LLIQ = 0.15500000000000005
ITER = 4.0
MDOT= 4.385407946470123E-7
MDOTROOT = 4.409922876974299E-7

REV = 121.61419707349204
REL = 10.478872034576161
QTOT= 0.9953345531113861
PCAP = 2617.777777777778
PTEMP = 10688.143735056057
PVAP = 11835.299766184986
PLIQ = 1407.9390893840782
PWIC= 62.682657264761005
++
MDOTMAX = 1.1899799999999997E-5
QTOTMAX = 27.008392969799992
****
LVAP= 0.16000000000000006
LLIQ = 0.16000000000000006
ITER = 4.0
MDOT= 4.248989463702909E-7
MDOTROOT = 4.2727397431891855E-7
REV = 117.8310999362981
REL = 10.152901944331923
QTOT= 0.9643723185282772
PCAP = 2617.777777777778
PTEMP = 10688.143735056057
PVAP = 11837.042357980585
PLIQ = 1408.1463898457762
PWIC= 60.73276500747195
++
MDOTMAX = 1.1899799999999997E-5
QTOTMAX = 27.008392969799992
****
LVAP= 0.16500000000000006
LLIQ = 0.16500000000000006
ITER = 4.0
MDOT= 4.120802169253837E-7
MDOTROOT = 4.1438339354099434E-7
REV = 114.27626647958508
REL = 9.846600165481092
QTOT= 0.935278276424914
PCAP = 2617.777777777778
PTEMP = 10688.143735056057
PVAP = 11838.679805656842
PLIQ = 1408.3411822579478
PWIC= 58.900524919104054
++
MDOTMAX = 1.1899799999999997E-5
QTOTMAX = 27.008392969799992
****
LVAP= 0.17000000000000007
LLIQ = 0.17000000000000007
ITER = 4.0
MDOT= 4.0001229026346064E-7
MDOTROOT = 4.0224782396687263E-7
REV = 110.92964233595693
REL = 9.558238715972777
QTOT= 0.9078882946087536
PCAP = 2617.777777777778
PTEMP = 10688.143735056057

PVAP = 11840.221346770935
PLIQ = 1408.5245655296262
PWIC= 57.175600533261395
++
MDOTMAX = 1.1899799999999997E-5
QTOTMAX = 27.008392969799992
****
LVAP= 0.175000000000000007
LLIQ = 0.175000000000000007
ITER = 4.0
MDOT= 3.88631080524007E-7
MDOTROOT = 3.9080282052016764E-7
REV = 107.77345549750609
REL = 9.286286272975078
QTOT= 0.8820569205423929
PCAP = 2617.777777777778
PTEMP = 10688.143735056057
PVAP = 11841.675167566606
PLIQ = 1408.6975135045504
PWIC= 55.54883176268269
++
MDOTMAX = 1.1899799999999997E-5
QTOTMAX = 27.008392969799992
****
LVAP= 0.180000000000000008
LLIQ = 0.180000000000000008
ITER = 4.0
MDOT= 3.778795935931658E-7
MDOTROOT = 3.79991069622200924E-7
REV = 104.79190060819907
REL = 9.02938096996812
QTOT= 0.8576547974783223
PCAP = 2617.777777777778
PTEMP = 10688.143735056057
PVAP = 11843.048548397126
PLIQ = 1408.8608922608219
PWIC= 54.01207217589229
++
MDOTMAX = 1.1899799999999997E-5
QTOTMAX = 27.008392969799992
****
LVAP= 0.185000000000000008
LLIQ = 0.185000000000000008
ITER = 4.0
MDOT= 3.677069725450325E-7
MDOTROOT = 3.697614292818188E-7
REV = 101.97087424987036
REL = 8.786307587694923
QTOT= 0.8345664979438056
PCAP = 2617.777777777778
PTEMP = 10688.143735056057
PVAP = 11844.347985659466
PLIQ = 1409.0154746163175
PWIC= 52.55805255804195
++
MDOTMAX = 1.1899799999999997E-5

QTOTMAX = 27.008392969799992
****
LVAP= 0.19000000000000009
LLIQ = 0.19000000000000009
ITER = 4.0
MDOT= 3.5806769322301057E-7
MDOTROOT = 3.6006812016971436E-7
REV = 99.29775186439561
REL = 8.555978332688424
QTOT= 0.8126886979912991
PCAP = 2617.777777777778
PTEMP = 10688.143735056057
PVAP = 11845.579294549685
PLIQ = 1409.1619523525728
PWIC= 51.18026593158239
+++
MDOTMAX = 1.1899799999999997E-5
QTOTMAX = 27.008392969799992
****
LVAP= 0.1950000000000001
LLIQ = 0.1950000000000001
ITER = 4.0
MDOT= 3.4892088311401583E-7
MDOTROOT = 3.508700406728498E-7
REV = 96.76119886689291
REL = 8.337416561864178
QTOT= 0.7919286312806091
PCAP = 2617.777777777778
PTEMP = 10688.143735056057
PVAP = 11846.747696068916
PLIQ = 1409.3009465650998
PWIC= 49.87287019981367
+++
MDOTMAX = 1.1899799999999997E-5
QTOTMAX = 27.008392969799992
****
LVAP= 0.2000000000000001
LLIQ = 0.2000000000000001
ITER = 4.0
MDOT= 3.402297420181505E-7
MDOTROOT = 3.4213018431780977E-7
REV = 94.3510099883945
REL = 8.129742939501803
QTOT= 0.7722027742012372
PCAP = 2617.777777777778
PTEMP = 10688.143735056057
PVAP = 11847.857891026433
PLIQ = 1409.4330164668684
PWIC= 48.63060534053117
+++
MDOTMAX = 1.1899799999999997E-5
QTOTMAX = 27.008392969799992
****

Appendix B - Process Flow for the Micro-CPL

1.0 Fabrication of Fluidic Channels

1.1 Single-Sided Polished Prime Wafer

1.2 Scribe Wafer

Wafers are scribed with lettering indicating the date they were placed into service, the run name, and the wafer number within that run. Scribing is done by hand using a diamond scribe.

1.3 Wet Thermal Oxidation

1.3.1 Standard Clean

10 Minutes 120 C Piranha bath (Sulfuric Acid with Hydrogen Peroxide).
De-ionized Water Rinse, 3 times, 1 minute each.
Dip until hydrophobic, 5:1 CMOS Grade Buffered Oxide Etch (J.T. Baker 5192-03, Ammonium Fluoride, Hydrofluoric Acid, Water).
De-ionized Water Rinse, 2 times, 1 minute each.
De-ionized Water Rinse until resistivity reaches 10.7 MΩ-cm.
Spin dry, 1 minute, 2400 RPM.

1.3.2 Standard Super-Clean

10 Minutes 120 C Piranha bath (Sulfuric Acid with Hydrogen Peroxide).
De-ionized Water Rinse, 3 times, 1 minute each.
Dip until hydrophobic, 10:1 VLSI Grade Hydrofluoric Acid.
De-ionized Water Rinse, 2 times, 1 minute each.
De-ionized Water Rinse until resistivity reaches 13.2 MΩ–cm.
Spin Dry, 1 minute, 2400 RPM.

1.3.3 Wet Oxidation

Wet thermal oxidation, 1100 C, 570 minutes, Nominal oxide thickness 2.0 μm.

1.4 Fluidic Channel Lithography

1.4.1 Standard Clean

10 Minutes 120 C Piranha bath (Sulfuric Acid with Hydrogen Peroxide).
De-ionized Water Rinse, 3 times, 1 minute each.
Dip until hydrophobic, 5:1 CMOS Grade Buffered Oxide Etch (J.T. Baker 5192-03, Ammonium Fluoride, Hydrofluoric Acid, Water).
De-ionized Water Rinse, 2 times, 1 minute each.
De-ionized Water Rinse until resistivity reaches 10.7 MΩ-cm.
Spin dry, 1 minute, 2400 RPM.

1.4.2 Dehydration

Dehydrate wafer in oven, 120 C, 20 minutes

1.4.3 HMDS

Apply HMDS using HMDS Bubbler, 5 minutes.

1.4.4 Photoresist Application
Apply STR 1075 positive resist on frontside of wafer. The application consists of 30 second
Spin at 5500 rpm followed 60 second soft bake on a 90 C hot plate. Nominal photoresist thickness is 8.0μm (before hard bake).

1.4.5 Expose
Full Wafer exposure using a Karl Suss Photolithography machine. Approximately 465mJ/cm^2 exposure.

1.4.6 Develop
Develop in microposit 452 developer. Three puddle develop, 120 seconds each. Rinse. Spin Dry 3500 rpm, 15 seconds.

1.4.7 Hard Bake
Oven at 120C for 40 minutes.

1.4.8 Lam Oxide Etch
Lam Research oxide etch, 850 Watt, 0.38 gap distance, 120 sccm Helium, 30 sccm CHF$_3$, 90 sccm CF$_4$.

1.4.9 Photoresist Strip
Soak, PRS 3000, 20 minute, 90 C. De-ionized Water Rinse, 3 times, 1 minute each. Spin dry, 1 minute, 2400 RPM.

1.5 Through-Hole Lithography

1.5.1 Standard Clean
10 Minutes 120 C Piranha bath (Sulfuric Acid with Hydrogen Peroxide).
De-ionized Water Rinse, 3 times, 1 minute each.
Dip until hydrophobic, 5:1 CMOS Grade Buffered Oxide Etch (J.T. Baker 5192-03, Ammonium Fluoride, Hydrofluoric Acid, Water).
De-ionized Water Rinse, 2 times, 1 minute each.
De-ionized Water Rinse until resistivity reaches 10.7 MΩ-cm.
Spin dry, 1 minute, 2400 RPM

1.5.2 Dehydration
Dehydrate wafer in oven, 120 C, 20 minutes

1.5.3 HMDS
Apply HMDS using HMDS Bubbler, 5 minutes.

1.5.4 Photoresist Application
Apply STR 1075 positive resist on frontside of wafer. Application consists of 30 second
Spin at 5500 rpm followed 60 second soft bake on a 90 C hot plate. Nominal photoresist thickness is 8.0μm (before hard bake).

1.5.5 Expose
Full Wafer exposure using a Karl Suss Photolithography machine. Approximately 465 mJ/cm^2 exposure.

1.5.6 Develop
Develop in microposit 452 developer. Three puddle develop, 120 seconds each. Rinse. Spin Dry 3500 rpm, 15 seconds. Repeat once more if necessary.

1.5.7 Hardbake
Oven at 120C for 60 minutes.
Let stand 15 minutes after hardbake.

1.6 Through-Hole STS Etch

1.6.1 STS Etch
Standard STS 25:1 Recipe, 400 μm etch.

1.6.2 Application of Backside Handle Wafer

1.6.2.1 Single-Sided Polished Prime Wafer

1.6.2.2 Dehydration
Dehydrate wafer in oven, 120 C, 20 minutes

1.6.2.3 HMDS
Apply HMDS using HMDS Bubbler, 5 minutes.

1.6.2.4 Photoresist Application
One application of OCG825 positive resist on frontside of wafer. Application consists of 30 second
Spin at 2200 rpm. Nominal photoresist thickness is 2.1 μm. Do not soft bake. Spin again at 5000 rpm
For edge bead removal.

1.6.2.5 Compression Bonding
Place handle wafer polished side up on a tech-wipe. Place the backside of the fluidic channel wafer in
contact with the frontside of the handle wafer, while visually aligning the flats of the two wafers. Place
another tech-wipe on top on the fluidic channel wafer. Gently press down.

1.6.2.6 Hard Bake
Oven at 120C for 40 minutes.

1.6.3 STS Etch
Standard STS 25:1 Recipe, 150 μm etch thus going all the way through the top wafer.

1.6.4 Photoresist Strip
Soak, PRS 3000, 20 minute, 90 C. De-ionized Water Rinse, 3 times, 1 minute each. Spin dry, 1 minute,
2400 RPM.

1.7 Fludic Channels STS ETCH

1.7.1 Standard Clean
10 Minutes 120 C Piranha bath (Sulfuric Acid with Hydrogen Peroxide).
De-ionized Water Rinse, 3 times, 1 minute each.
Dip until hydrophobic, 5:1 CMOS Grade Buffered Oxide Etch (J.T. Baker 5192-03, Ammonium Fluoride,
Hydrofluoric Acid, Water).
De-ionized Water Rinse, 2 times, 1 minute each.
De-ionized Water Rinse until resistivity reaches 10.7 MΩ-cm.
Spin dry, 1 minute, 2400 RPM.

95

1.7.2 Application of Backside Handle Wafer

1.7.2.1 Single-Sided Polished Prime Wafer

1.7.2.2 Dehydration
Dehydrate wafer in oven, 120 C, 20 minutes

1.7.2.3 HMDS
Apply HMDS using HMDS Bubbler, 5 minutes.

1.7.2.4 Photoresist Application
One application of OCG825 positive resist on frontside of wafer. Application consists of 30 second
Spin at 2200 rpm. Nominal photoresist thickness is 2.0μm. Do not soft bake. Spin again at 5000 rpm
For edge bead removal.

1.7.2.5 Compression Bonding
Place handle wafer polished side up on a tech-wipe. Place the backside of the fluidic channel wafer in
contact with the frontside of the handle wafer, while visually aligning the flats of the two wafers. Place
another tech-wipe on top on the fluidic channel wafer. Gently press down.

1.7.2.6 Hard Bake
Oven at 120C for 40 minutes.

1.7.3 STS Etch
Standard STS 25:1 Recipe, 150 μm etch.

1.7.4 Photoresist Strip
Soak, PRS 2300, 20 minute, 90 C. De-ionized Water Rinse, 3 times, 1 minute each. Spin dry, 1 minute,
2400 RPM.

1.8 End Fluidic Channels Fabrication

2.0 Glass Coverplate with Wicking Structure

2.1 Standard Burofloat Glass Wafer

2.2 Umpdoped Polysilicon LPCVD
2.2.1 Standard Clean
10 Minutes 120 C Piranha bath (Sulfuric Acid with Hydrogen Peroxide).
De-ionized Water Rinse, 3 times, 1 minute each.
De-ionized Water Rinse until resistivity reaches 10.7 MΩ-cm.
Spin dry, 1 minute, 2400 RPM.

2.2.2 Undoped Polysilicon Low Pressure Chemical Vapor Deposition
Deposit for 25 Ohms/square layer. Temperature 550 C, 100 sccm SiH_4 at a pressure of 300 mT ,
approximately 4 Hours for 1μm layer.

2.3 Wicking Structure Lithography

2.3.1 Standard Clean
10 Minutes 120 C Piranha bath (Sulfuric Acid with Hydrogen Peroxide).
De-ionized Water Rinse, 3 times, 1 minute each.
De-ionized Water Rinse until resistivity reaches 10.7 MΩ-cm.
Spin dry, 1 minute, 2400 RPM

2.3.2 Dehydration
Dehydrate wafer in oven, 120 C, 20 minutes

2.3.3 HMDS
Apply HMDS using HMDS Bubbler, 5 minutes.

2.3.4 Photoresist Application
Apply one layer of 1075 STR positive resist on frontside of wafer. Each application consists of 30 second
Spin at 5500 rpm followed 60 second soft bake on a 90 C hot plate. Nominal photoresist thickness is
8.0 μm (before hard bake).

2.3.5 Expose
Full Wafer exposure using a Karl Suss Photolithography machine. Approximately 465 mJ/cm^2 exposure.

2.3.6 Develop
Develop in microposit 452 developer. Three puddle develop, 120 seconds each. Rinse. Spin Dry 3500 rpm,
15 seconds.

2.3.7 Hardbake
Oven at 120C for 40 minutes.

2.3.8 Place DISCO Tape on Backside of Wafer

2.3.9 Dry Etch in CH$_4$
Place wafer in Technics plasma etcher. Flow CH$_4$ at 280 mT, at a power of 200 W for 9 minutes.

2.3.10 Standard Clean
10 Minutes 120 C Piranha bath (Sulfuric Acid with Hydrogen Peroxide).
De-ionized Water Rinse, 3 times, 1 minute each.
De-ionized Water Rinse, 2 times, 1 minute each.
De-ionized Water Rinse until resistivity reaches 10.7 MΩ-cm.
Spin dry, 1 minute, 2400 RPM

2.3.11 Photoresist Strip
Soak, PRS 3000, 20 minute, 90 C. De-ionized Water Rinse, 3 times, 1 minute each. Spin dry, 1 minute,
2400 RPM.

2.4 Wet Etching of the Wicking Structure

2.4.1 Wet Etch in Concentrate Hydroflouric Acid
Place wafer in 49% VLSI Grade Hydroflouic Acid for 6 minutes (until a depth of 50 μm has been
Attained.)

2.4.2 Standard Clean
10 Minutes 120 C Piranha bath (Sulfuric Acid with Hydrogen Peroxide).
De-ionized Water Rinse, 3 times, 1 minute each.
De-ionized Water Rinse, 2 times, 1 minute each.
De-ionized Water Rinse until resistivity reaches 10.7 MΩ-cm.
Spin dry, 1 minute, 2400 RPM

2.4.3 Polysilicon Strip
Place wafer in 1890 ml Nitric Acid, 960 ml De-ionized water, and 75 ml Ammonium Fluoride until
   All Polysilicon has been removed from the wafer.

2.4.4 Standard Clean
10 Minutes 120 C Piranha bath (Sulfuric Acid with Hydrogen Peroxide).
De-ionized Water Rinse, 3 times, 1 minute each.
De-ionized Water Rinse, 2 times, 1 minute each.
De-ionized Water Rinse until resistivity reaches 10.7 MΩ-cm.
Spin dry, 1 minute, 2400 RPM

2.5   End Coverplate Fabrication

3.0 Device Assembly

3.1 Start with Channel Wafer (Silicon) and Coverplate (Glass)

3.2 Anodic Bond Preparation

3.2.1 Standard Clean of Silicon Wafer
10 Minutes 120 C Piranha bath (Sulfuric Acid with Hydrogen Peroxide).
De-ionized Water Rinse, 3 times, 1 minute each.
Dip until hydrophobic, 5:1 CMOS Grade Buffered Oxide Etch (J.T. Baker 5192-03, Ammonium Fluoride,
   Hydrofluoric Acid, Water).
De-ionized Water Rinse, 2 times, 1 minute each.
De-ionized Water Rinse until resistivity reaches 10.7 MΩ-cm.
Spin dry, 1 minute, 2400 RPM.

3.2.2   Standard Super-Clean of Silicon Wafer
10 Minutes 120 C Piranha bath (Sulfuric Acid with Hydrogen Peroxide).
De-ionized Water Rinse, 3 times, 1 minute each.
Dip until hydrophobic, 10:1 VLSI Grade Hydrofluoric Acid (Channel wafer only)
De-ionized Water Rinse, 2 times, 1 minute each.
De-ionized Water Rinse until resistivity reaches 13.2 MΩ–cm.
Spin Dry, 1 minute, 2400 RPM.

3.2.3   Standard Clean of Glass Wafer
10 Minutes 120 C Piranha bath (Sulfuric Acid with Hydrogen Peroxide).
De-ionized Water Rinse, 3 times, 1 minute each.
De-ionized Water Rinse until resistivity reaches 10.7 MΩ-cm.
Spin dry, 1 minute, 2400 RPM

3.2.3 Align Wafers

Using a Karl Suss wafer aligner, match up the alignment marks on the Channel wafer (placed on top
And upside down) to the complimentary alignment marks on the glaSS wafer. Lock these into
Position in the wafer holder and remove from machine.

3.3 Anodic Bond

Place wafer holder with aligned wafers into Karl Suss Wafer Bonder. Anodic Bond with −1500 V (polarity
is negative because glass is on top), at 375 C.

3.4 End Assembly

4.0 Hydrophobic Coating of Silicon Wafer

4.1   1H,1H,2H,2H-perfluorodecyltrichlorosilane (FDTS) Self Assembled
Monolayer Coating (SAM)

Place 2 drops of FDTS in 140ml of Iso-Octane for 15 minutes
Flow solution over Silicon Wafer for 20 minutes using a needle in the through-holes.
Flow pure Iso-Octane over wafer for 15 minutes using a needle in the through-holes.
Flow Iso-proponal over wafer for 15 minutes using a needle in the through-holes.
Flow de-ionized water over wafer for 15 minutes using a needle in the through-holes.